# Impact of methane and other precursor emission reductions on surface ozone in Europe: Scenario analysis using the EMEP MSC-W model

Willem E. van Caspel[1], Zbigniew Klimont[2], Chris Heyes[2], and Hilde Fagerli[1]

[1]EMEP MSC-W, Norwegian Meteorological Institute, Oslo, Norway
[2]International Institute for Applied Systems Analysis, Laxenburg, Austria

**Correspondence:** W.E. van Caspel (willemvc@met.no)

**Abstract.**

The impacts of future methane ($CH_4$) and other precursor emission changes are investigated for surface ozone ($O_3$) in the United Nations Economic Commission for Europe (UNECE) region excluding North America and Israel (the "EMEP region", for European Monitoring and Evaluation Programme) for the year 2050. The analysis includes a Current Legislation (CLE) and Maximum Feasible Technical (MFR) reduction scenario, and a scenario that combines MFR reductions with an additional dietary shift that also meets the Paris Agreement objectives with respect to greenhouse gas emissions (LOW). For each scenario, background $CH_4$ concentrations are calculated using a probabilistic Earth System model emulator, and combined with other precursor emissions in a three-dimensional Eulerian chemistry-transport model. While focus is placed on peak season maximum daily 8-hour average (MDA8) $O_3$ concentrations, a range of other indicators for health and vegetation impacts are also discussed. Our analysis show that roughly one-thirds of the total peak season MDA8 reduction achieved between the 2050 CLE and MFR scenarios is attributable to $CH_4$ reductions, resulting predominantly from $CH_4$ emission reductions outside of the EMEP region. The impact of other precursor emission reductions is split nearly evenly between the reductions inside and outside of the EMEP region. However, the relative importance of $CH_4$ and other precursor emission reductions is shown to depend on the choice of $O_3$ indicator, though indicators sensitive to peak $O_3$ show generally consistent results. The analysis also highlights the synergistic impacts of $CH_4$ mitigation as reducing solely $CH_4$ achieves, beyond air quality improvement, nearly two-thirds of the total global warming reduction calculated for the LOW scenario compared to the CLE case.

**Plain language summary**

Methane in the atmosphere contributes to the production of ozone gas, which is an air pollutant as well as a greenhouse gas. In this study, the impact of reducing methane emissions on surface ozone is investigated for the United Nations Economic Commission for Europe (UNECE) region excluding North America and Israel (the "EMEP region"), in particular in terms of its importance in reaching the ozone exposure guideline limits set by the World Health Organization. The relative importance of reducing emissions of other pollutants that lead to the formation of ozone, such as nitrogen oxides, is also investigated. To this end, our study employs emission scenarios up to the year 2050, each having different assumptions about future human-caused emissions. Relative to a scenario where only the already agreed emission reductions are implemented, one-third of surface ozone reductions in the most ambitious emission reduction scenario are attributable to methane reductions. The other two-thirds are attributable to emission reductions of other ozone forming pollutants, with reductions inside and outside of the EMEP region contributing roughly equally.

# 1 Introduction

30 Surface ozone ($O_3$) is an important source of air pollution, impacting both human and ecosystem health (Lefohn et al., 2018; Monks et al., 2015). In the lower troposphere, the majority of $O_3$ is produced by the photochemical reaction of nitrogen oxides ($NO_x = NO + NO_2$) in Volatile Organic Compound (VOC) rich environments (Crutzen et al., 1999). The most abundant VOC precursor species is methane ($CH_4$), having a present-day volume mixing ratio of around 1915 parts-per-billion (ppb) (Lan et al., 2024). Moreover, $CH_4$ mixing ratios are likely to increase further, as anthropogenic $CH_4$ emissions are anticipated to

35 increase in the coming decade (UNEP, 2021; Saunois et al., 2020; Höglund-Isaksson et al., 2020). In addition to being a source of air pollution, $CH_4$ is also the second most important anthropogenic greenhouse gas (GHG), with its importance as both an air pollutant and global warming agent having received considerable attention in recent years (Mar et al., 2022; Abernethy et al., 2021; Fiore et al., 2008; Dentener et al., 2005).

In this study, the impact of $CH_4$ and other precursor emissions is investigated for the European Monitoring and Evaluation

40 Programme (EMEP) region, which includes the member countries of the United Nations Economic Commission for Europe (UNECE) region excluding North America and Israel. Focus is placed on the population-weighted exposure to peak season (April-September) average maximum daily 8-hour mean (MDA8) $O_3$ concentrations, being the health indicator employed by the new World Health Organization (WHO) guidelines (WHO, 2021). The latter recommends a peak season MDA8 exposure limit of 60 µg m$^{-3}$ based on the association between long-term $O_3$ exposure and all-cause mortality, with an interim target of

45 70 µg m$^{-3}$ for areas where initial exposure is high. To our knowledge, neither the guideline nor interim target values are met in any of the countries within the EMEP region at present. In addition to being employed by the WHO, the focus on peak season MDA8 is also motivated by the broader association between the exposure to peak $O_3$ and all-cause mortality (Huangfu and Atkinson, 2020).

The impacts on $O_3$ are investigated for a Current Legislation (CLE), Maximum technical Feasible Reduction (MFR), and

50 MFR with an additional dietary shift and Paris Agreement policy scenario (LOW) up to the year 2050. The CLE scenario includes the currently agreed upon policies for the abatement of air pollutant and GHG emissions, while the MFR scenario combines the economic activity pathway of the CLE scenario with the full implementation of the best available emission reduction technologies defined in the GAINS (Greenhouse gas – Air pollution Interactions and Synergies) model (Amann et al., 2011). The LOW scenario extends the MFR by including climate policies compatible with the Paris Agreement objectives and

55 an additional shift in agricultural practices, bringing further $CH_4$ and other precursor emission reductions. Relative to the year 2015, global anthropogenic $CH_4$ emissions decline by 35 % and 50 % in the LOW scenario by 2030 and 2050, respectively, making the reductions comparable to those of the Methane Pledge (30 % by 2030, Malley et al., 2023) and Global Methane Assessment (45 % abatement target for 2050, UNEP, 2021).

The emission scenarios are combined with the Model for the Assessment of Greenhouse-gas Induced Climate Change v7.5.3

60 (MAGICC7) (Meinshausen et al., 2020, 2011, 2009) to calculate their respective background $CH_4$ concentrations up to the year 2050. To calculate the impacts on surface $O_3$, the $CH_4$ projections are specified in the three-dimensional Eulerian Chemistry-Transport Model (CTM) developed at the EMEP Meteorological Synthesising Centre – West (hereafter "EMEP model"), where

they are also combined with the other precursor scenario emissions. The EMEP model has a long history of policy support and research development (e.g., Jonson et al., 2018; Simpson, 2013; Simpson et al., 2012), with one of its main tasks being the modeling of transboundary fluxes of air pollutants as part of the UNECE Convention on Long-range Transboundary Air Pollution (CLRTAP) (Fagerli et al., 2023). In this capacity, the EMEP model has previously been used in support of the review of the UNECE Gothenburg Protocol (Protocol to Abate Acidification, Eutrophication and Ground-level Ozone). The current work in part aims to contribute to the discussion surrounding the second revision of the Gothenburg Protocol, for which the impact of $CH_4$ on surface $O_3$ plays a prominent role.

The emission scenarios and their implementation are described in more detail Sect. 2. The MAGICC7 model is described in Sect. 3, where it is also used to calculate background $CH_4$ concentrations up to the year 2050. Sect. 4 describes the EMEP model configuration, while also evaluating the baseline configuration against five years of observations across Europe. For the scenario calculations presented in Sect. 5, the default modeling configuration involves averaging all results over five meteorological years, while a linear latitudinal $CH_4$ gradient is imposed to capture the effects of inter-hemispheric variations in emissions. Sect. 5 further combines regional EMEP model simulations with global simulations to quantify the separate impacts of emission changes inside and outside of the EMEP region. While focus is placed on the peak season MDA8 indicator, scenario results for a range of other $O_3$ health and vegetation indicators are also presented. The results are discussed and compared against earlier studies in Sect. 6, followed by a conclusion in Sect. 7.

## 2    Emissions

The emission scenarios were developed using the global version of the GAINS model (Winiwarter et al., 2018; Klimont et al., 2017; Höglund-Isaksson, 2012; Amann et al., 2011), and provided by the EMEP Center for Integrated Assessment Modelling (CIAM) hosted by the Institute for Applied Systems Analysis (IIASA). The scenarios include annual anthropogenic emission totals of $CH_4$, $NO_x$, Non-Methane Volatile Organic Compounds (NMVOC), carbon monoxide (CO), sulphur oxides ($SO_x$), ammonia ($NH_3$), primary fine Particulate Matter ($PM_{2.5}$), and primary coarse PM ($PM_{co}$), as well as the carbonaceous fraction of primary PM represented by black carbon (BC) and organic carbon (OC). In the context of the current work, the key emission species are $CH_4$, $NO_x$, CO, and NMVOC, where the latter three affect the lifetime of $CH_4$ by acting as either net sources ($NO_x$) or sinks (CO and NMVOC) of hydroxyl (OH). OH in turn affects the lifetime of $CH_4$ by loss against oxidation. The global emission totals for the key species are shown in Table 1, along with their respective emissions within the EMEP region for the years 2015, 2030, and 2050.

The emission scenarios span the period from the baseline year 2015 up to 2050 in 5-year intervals, with the MFR and LOW scenarios diverging from the CLE scenario from 2025 onwards. The latter is motivated by the political process of agreeing upon, and enforcing effective implementation of, the proposed emission control strategies taking at least a few years. 2026 being the first year where annual emission totals differ can therefore be considered an optimistic target. In the EMEP model, natural emissions of soil $NO_x$ are included based on monthly climatological values from the CAMS-GLOB-SOIL v2.4 inventory (Simpson and Darras, 2021), noting that soil $NO_x$ emissions from the application of manures and mineral nitrogen fertilizers on agricultural land are calculated in the GAINS model. Forest fire emissions are included based on the daily Fire INventory from NCAR version 2.5 (FINNv2.5, Wiedinmyer et al., 2023) dataset, derived from fire detections from both the Moderate Resolution Imaging Spectroradiometer (MODIS) and Visible Infrared Imaging Radiometer Suite (VIIRS) satellite instruments. Forest fire emissions are kept fixed to that of the simulation's meteorological year, also for the future scenario calculations.

### 2.1    Emission scenarios

#### 2.1.1    CLE scenario

The CLE scenario assumes the implementation and effective enforcement of all currently committed energy and environmental policies affecting emissions of air pollutants and greenhouse gases. CIAM has undertaken a review and update of historical data (up to 2020) driving emissions of all species in the GAINS model, drawing on information from the statistical office of the European Union (EUROSTAT), International Energy Agency (IEA), and UN Food and Agriculture Organization (FAO), in addition to data and emissions reported to the Center on Emission Inventories and Projections (CEIP). For the EU27 countries, the energy and agriculture projections are consistent with the objectives of the European Green Deal and 'Fit for 55' package to make the EU carbon neutral by 2050, while also being consistent with the projections used in the EU 3rd Clean Air Outlook (https://environment.ec.europa.eu/topics/air/clean-air-outlook_en, last access: April 2024). For the West Balkan, Republic of Moldova, Georgia, and Ukraine, a similar set of modelling tools was used as for the EU, developing a new consistent set of projections. For other world regions, the GAINS model down-scales projections from IEA and FAO (Alexandratos and

**Table 1.** Global emission totals for the CLE, MFR, and LOW emission scenarios in units of Tg yr$^{-1}$. Emission totals within the EMEP region, as defined in Sect. 1, are listed in brackets for the years 2015, 2030, and 2050. $NO_x$ emissions have a molecular weight of 46 g mol$^{-1}$.

| Species | Scenario | 2015 | 2020 | 2025 | 2030 | 2035 | 2040 | 2045 | 2050 |
|---------|----------|------|------|------|------|------|------|------|------|
| $NO_x$ | CLE | 119 (16) | 111 | 106 | 103 (10) | 102 | 103 | 104 | 106 (9) |
| $NO_x$ | MFR | | | | 65 (6) | 52 | 42 | 40 | 38 (4) |
| $NO_x$ | LOW | | | | 62 (6) | 46 | 33 | 29 | 25 (3) |
| NMVOC | CLE | 121 (15) | 120 | 120 | 118 (14) | 119 | 119 | 120 | 121 (14) |
| NMVOC | MFR | | | | 68 (10) | 63 | 59 | 59 | 59 (8) |
| NMVOC | LOW | | | | 63 (9) | 57 | 52 | 50 | 48 (8) |
| CO | CLE | 517 (50) | 474 | 449 | 427 (37) | 418 | 411 | 408 | 405 (43) |
| CO | MFR | | | | 160 (22) | 139 | 123 | 123 | 123 (18) |
| CO | LOW | | | | 149 (22) | 124 | 102 | 96 | 91 (17) |
| $CH_4$ | CLE | 334 (62) | 345 | 360 | 371 (60) | 385 | 401 | 416 | 428 (60) |
| $CH_4$ | MFR | | | | 229 (28) | 224 | 226 | 220 | 210 (22) |
| $CH_4$ | LOW | | | | 219 (27) | 208 | 202 | 195 | 168 (14) |

Bruinsma, 2012; IEA, 2018), considering updated air pollution legislation from national and international sources (e.g., He et al., 2021; Zhang, 2018), including EU legislation and their implementation in consultation with the EU Member States. For the CLE scenario, the socio-economic activity assumptions are similar to that of the Shared Socioeconomic Pathway 2 with an end-of-century radiative forcing of 4.5 W m$^{-2}$ (SSP2-4.5). The SSP2-4.5 scenario describes the 'middle of the road' for future societal development, as described in Meinshausen et al. (2020), O'Neill et al. (2017), and Riahi et al. (2017) for a range of SSP scenarios. For the background $CH_4$ calculations described in Sect. 3, the CLE scenario emissions are therefore combined with GHG emissions (e.g., $CO_2$ and hydrofluorocarbons) from the SSP2-4.5 scenario. We note that the CLE scenario used in this work does not include the impact of recent shock events (e.g., COVID-19).

### 2.1.2 MFR mitigation scenario

The MFR mitigation scenario assumes the full implementation of the proven technical mitigation potential as included in the GAINS model for precursor emissions (Amann et al., 2020, 2013; Rafaj et al., 2018) and $CH_4$ (Gomez Sanabria et al., 2022; Höglund-Isaksson et al., 2020; Höglund-Isaksson, 2012). Technologies to abate air pollution precursor emissions include, for example, end of pipe technologies applied in the power, industry, and transport sector, technology change in industry and residential combustion, as well as measures in agriculture addressing emissions from manures and mineral fertilizer application by, for example, improved manure management techniques and the construction of low emission housing including covered manure stores. The fossil fuel and solvent sector emissions include improved flaring, maintenance, leakage, and distribution control measures, as well as low-solvent product substitutions. Global emissions of $NO_x$, NMVOC, and CO decline by nearly

80 % by 2050 relative to the 2015 baseline, while $CH_4$ emissions fall by 37 %. These reductions are driven by the rapid introduction of stringent emission limit values for stationary and mobile sources, strong decline in fossil fuel use, and access to clean energy for cooking. The MFR energy and agricultural activity projections are the same as those of the CLE scenario, with the MFR scenario also being combined with GHG emissions from the SSP2-4.5 scenario.

### 2.1.3  LOW mitigation scenario

The LOW mitigation scenario extends the MFR by including several additional policies targeting significant transformations in the agricultural sector. This transformation leads to strong reductions of livestock numbers, especially cattle and pigs. The scenario is based in part on the 'Growing Better report 2019' (The Food and Land Use Coalition, 2019) and other studies addressing healthy dietary requirements (Kanter et al., 2020; Willett et al., 2019), as used in earlier scenarios for global air pollution studies (Amann et al., 2020). While the LOW scenario has the same energy projections as the CLE for EU27 countries, the rest of the world now includes climate policies compatible with Paris Agreement goals, making the GHG emissions consistent with those of the 'taking the green road' SSP1-2.6 scenario (Riahi et al., 2017; O'Neill et al., 2017). In the LOW scenario, global $CH_4$ emission decline by 34 % and 50 % relative to the 2015 baseline by 2030 and 2050, respectively.

### 2.2  Model implementation

The annual mean national and sector (e.g., road traffic and agriculture) emission totals are distributed in time using a set of monthly, weekly, daily, and hourly time-factors based on the global and European CAMS-TEMPO datasets described in Guevara et al. (2021, 2020a, b). For the regional EMEP modelling domain discussed in Sect. 4, the native $0.5° \times 0.5°$ scenario emissions are redistributed to the $0.1° \times 0.1°$ spatial distribution of the most recent EMEP reported emissions (2021) for countries within the EMEP region (EMEP/CEIP, 2023). However, following the approach used for the first Gothenburg Protocol review, native $0.1° \times 0.1°$ gridded emissions from CIAM are used for countries located within the West-Balkan and Economic Co-operation and Development, Eastern Europe, Caucasus and Central Asia (EECCA) regions, and for Türkiye. Countries that lie (partially) within the regional modelling domain but that are not part of the EMEP region, such as North African countries, follow the global $0.5° \times 0.5°$ gridded emissions. International shipping emissions also follow the global $0.5° \times 0.5°$ spatial distribution provided by CIAM for all simulations. We further note that direct emissions of $CH_4$ are not included in the EMEP model, with concentrations instead being specified on an annual mean basis, as discussed in Sect. 4.

# 3 Background CH$_4$

Earth System emulators, sometimes known as Reduced Complexity Models (RCMs), have a long history of development as low-cost alternatives to full complexity climate models. RCMs include simplified parameterizations of, for example, ocean heat uptake, GHG effective radiative forcing, and climate feedbacks, to efficiently estimate future change in climate variables such as GHG concentrations and global-mean surface air temperature (GSAT) (Nicholls et al., 2021, 2020). To this end, the MAGICC7 v7.5.3 RCM has been used in the Intergovernmental Panel on Climate Change (IPCC) Sixth Assessment Report (AR6) (Forster et al., 2021), being calibrated to capture the relationship between emissions and GSAT for the AR6 historical temperature assessment (Nicholls et al., 2022). In the current work, the MAGGIC7 model is run using the 5-yearly annual emission totals from Table 1, linearly interpolated to annual values and combined with their respective SSP GHG scenario emissions.

In the MAGICC7 model, CH$_4$ sinks are represented by loss against OH in the troposphere, loss to the stratosphere, and soil uptake (Meinshausen et al., 2011). Climate sensitivities for these mechanisms arise from, for example, temperature-driven changes in atmospheric composition, changes in the Brewer-Dobson circulation strength, and changing soil properties. CH$_4$ sources are controlled by the separate contributions arising from anthropogenic, natural, and permafrost emissions. Permafrost is assumed start thawing when global mean temperatures rise 1 degree K above pre-industrial levels, with the permafrost module incorporating effects such as polar amplification, soil specific thawing and decomposition rates, and soilwater uptake (Schneider von Deimling et al., 2012). Natural emissions are estimated by closing the CH$_4$ budget between the years 2015-2023, for which the IIASA emissions are the same for all scenarios, using observed global mean background CH$_4$ concentrations up to the most recent year for reference (1923 ppb by 2023, Lan et al., 2024). With this approach, natural emissions are estimated at 214.9 Tg yr$^{-1}$, falling within the top-down range of 194–267 Tg yr$^{-1}$ reported by Saunois et al. (2020) for the year 2017. The natural emissions are kept constant throughout the simulation period.

A key feature of the MAGICC7 model is that it can be run in a probabilistic mode, where the results of its 600-member ensemble reflect the uncertainties in the parameters controlling future climate change (Nicholls et al., 2022). However, the initial parameter values controlling the CH$_4$-cycle are the same for each ensemble run, with parameters such as the initial lifetime of CH$_4$ (9.95 yr$^{-1}$) and temperature-sensitivity of the loss against OH (0.07 K$^{-1}$) calibrated to match the projections by Holmes et al. (2013) across the range of Representative Concentration Pathway (RCP) scenarios (Meinshausen et al., 2020). As a result, the inter-ensemble variations for the calculated CH$_4$ projections represent the sensitivity of the different CH$_4$ source and sink terms to temperature change. We note that the net land-to-atmosphere CH$_4$ flux from permafrost is found to make a relatively small contribution to the ensemble simulation results, with its 600-ensemble mean emissions falling below 4 Tg yr$^{-1}$ by 2050 for all scenarios. Nevertheless, its 5-95 % range amounts to 0.5–11.2 Tg yr$^{-1}$ in the 2050 CLE scenario, compared to a 0.1-2.3 Tg yr$^{-1}$ range in 2015. Thus illustrating that permafrost emissions can increase by 9 Tg yr$^{-1}$ for some ensemble members, representing a 4-5 % increase in total natural emissions.

## 3.1 $CH_4$ projections

Fig. 1 shows the $CH_4$ projections calculated for the CLE, MFR, and LOW scenarios, with the shaded regions indicating the the 5th to 95th percentile (5-95 %) range of the 600-ensemble model output. Here the $CH_4$ projections for the SSP1-2.6, SSP2-4.5, and SSP5-8.5 scenarios are also included for reference, noting that the IIASA scenario projections fall within the range of the optimistic (SSP1-2.6) and pessimistic (SSP5-8.5) scenarios. While the SSP3-7.0 scenario is the most pessimistic in terms of $CH_4$ emissions (Meinshausen et al., 2020), its calculated $CH_4$ concentrations only begin to diverge from the SSP5-8.5 scenario roughly from 2060 onward, and is therefore not discussed here. For the CLE, MFR, and LOW scenarios, the 2050 global mean $CH_4$ concentrations and their 5-95 % range are calculated as 2236 [2166-2299], 1651 [1597-1700], and 1574 [1512-1627] ppb, respectively. For other years, ensemble mean $CH_4$ concentrations are shown in supplementary Table S1.

Fig. 1 shows that the (temperature-driven) MFR and LOW scenarios uncertainties partly overlap. However, the inter-scenario difference between the CLE and the MFR (and LOW) scenarios far exceeds the temperature-driven uncertainties, with the 2050 ensemble mean difference amounting to 585 ppb. In the current work, the difference between the 2050 CLE and the MFR scenarios represents an important measure of the impact of $CH_4$ emission changes, as this represents the largest inter-scenario concentration difference. While both scenarios have a 5-95 % range of approximately 100 ppb by 2050, the 5-95 % interval of the difference between the 2050 CLE and MFR scenarios amounts to 571-598 ppb. Thus illustrating that ensemble members with a comparatively high $CH_4$ concentration in the CLE scenario also have a comparatively high concentration in the MFR scenario, and that the ensemble mean scenario difference of 585 ppb is therefore robust.

Diagnostic simulations for a scenario where $CH_4$ emissions follow the LOW scenario while all other emissions follow those of the CLE scenario (LOW-$CH_4$) are also performed. This hypothetical scenario thereby reflects a situation where $CH_4$ emissions are reduced strongly, while no further abatement policies are implemented for the other emissions. In reality, however, $CH_4$ reductions likely also lead to a reduction in other co-emitted species. The resulting 2050 LOW-$CH_4$ concentration of 1440 [1392-1484] ppb is comparable to that of the LOW scenario, although lower by 134 ppb (-8.5 %) due to the higher emissions of other lifetime-affecting precursor species. The LOW-$CH_4$ scenario thereby illustrates that the difference in $CH_4$ concentrations between the 2050 CLE and LOW scenarios (and corollary MFR) is primarily driven by the difference in the direct emissions of $CH_4$, and to a lesser extent by the difference in other precursor emissions. A diagnostic LOW scenario where the other GHGs are based on SSP2-4.5 rather than SSP1-2.6, find that the GHGs from the SSP1-2.6 scenario have very little impact on the simulated $CH_4$ concentrations (< 4 ppb difference by 2050 for all ensemble members). We further note that continuing the $CH_4$ projections into 2055 with the emissions fixed to that of 2050 leads to an additional change in the ensemble-mean concentrations of 38 ppb (1.7 %), -45 ppb (-2.7 %), and -70 ppb (-4.45 %) for the CLE, MFR, and LOW scenarios, respectively. The latter illustrates that, as expected, the $CH_4$ source and sink terms have not yet reached equilibrium by 2050, owing to the relatively long lifetime of $CH_4$.
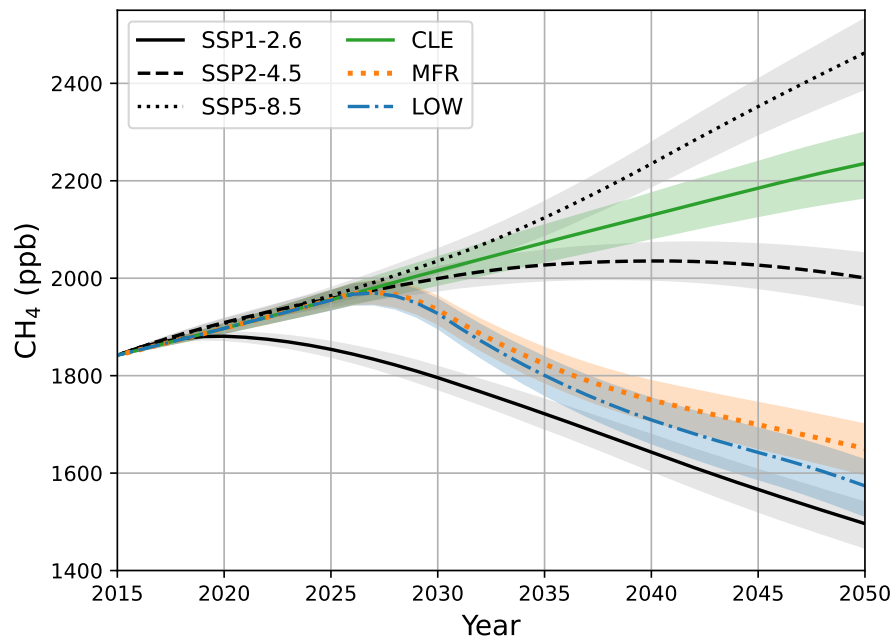
**Figure 1.** Projected background $CH_4$ concentrations up to 2050 for the CLE, MFR, and LOW scenarios described in the text. Projections for the SSP5-8.5, SSP2-4.5, and SSP1-2.6 scenarios are included for reference. Shaded areas represent the 600-ensemble 5-95 % range.

## 4 EMEP model description

The current work uses EMEP model version rv5.3, as described in more detail by EMEP MSC-W (2023) (for Meteorological Synthesing Centre – West) and others (e.g., Ge et al., 2024; van Caspel et al., 2023; Stadtler et al., 2018; Simpson et al., 2012). The model employs 20 vertical hybrid pressure-$\sigma$ levels for the regional $0.1° \times 0.1°$ EMEP modelling domain (30°N-82°N, 30°W-90°E), and 19 vertical levels for the global $0.5° \times 0.5°$ modelling domain. Both the regional and global grids use 3-hourly meteorological data derived from the ECMWF Integrated Forecasting System (IFS) cycle 40r1 model (ECMWF, 2014). The EMEP model uses its default EmChem19 mechanism (Bergström et al., 2022), designed to balance computational complexity with realism by employing a simplified set of lumped VOC species (Ge et al., 2024). In EmChem19, $NO_x$ is emitted with a 95:5 ratio for $NO_2$:NO over land areas. Over pristine maritime environments, half the $NO_x$ emissions are instead placed in a ShipNO$_x$ psuedo-species and chemically converted to $HNO_3$ to capture the effects of ship plume chemistry (Simpson et al., 2015). While the EMEP model and its chemistry are fully time-dependent, background $CH_4$ and $H_2$ concentrations are specified at the start of each run and kept fixed throughout the simulation period. However, the chemistry involved with the latter species (e.g., loss of OH and the subsequent chain of reactions leading to $O_3$ formation from the oxidation of $CH_4$) remains fully interactive. Hydrogen gas ($H_2$) is specified with a fixed global concentration of 500 ppb.

In the EMEP model, 3-hourly IFS $O_3$ concentrations are specified at the model top (100 hPa) boundary condition, while output surface concentrations are adjusted to an equivalent altitude of 3 meters. For the lateral boundary conditions (LBCs) in the regional simulations, 6-hourly output fields from global simulations are used, with each of the global simulations employing a spin-up period of six months. Diagnostic simulations find that the choice of LBC time-resolution has a negligibly small impact on the simulation results, while choosing 6-hourly over 3-hourly LBCs saves considerable computation time. Output fields from the global model are also used as initial conditions for the regional runs. The geographical region spanned by the regional EMEP modelling domain contains the EMEP region, but also parts of North Africa and Asia, whose emissions are consistently treated as Rest-Of-World (ROW) between the global and regional simulations. For reference, the EMEP region as represented in the regional EMEP modelling domain is shown in supplementary Fig. S1.

### 4.1 CH$_4$ implementation

As discussed above, global mean $CH_4$ concentrations are specified at the start of each run and remain unchanged over the course of the simulation. However, observed $CH_4$ concentrations display a marked latitudinal gradient, primarily due to the presence of large natural and anthropogenic emission sources in the Northern Hemisphere. The latitudinal gradient can be described by its two leading Empirical Orthogonal Functions (EOFs), or principal components (Meinshausen et al., 2017). The first EOF (EOF1) represents a nearly linear North-South gradient, while the second EOF (EOF2) represents a local northern mid-latitude maximum of ∼10 ppb. EOF1 has a pre-industrial North to South pole gradient of around 40-50 ppb, and of around 90 ppb for the year 2014 (Meinshausen et al., 2017). To capture the main characteristics of the latitudinal gradient, the contribution of EOF1 is included in the EMEP model by specifying

**Table 2.** EMEP model configurations for the scenario analysis discussed in Sect. 5. The $CH_4$ concentrations refer to the 2050 global mean values calculated in Sect. 3. Each of the scenarios is simulated for the five meteorological years between 2013-2017.

| Experiment long-name | Short-name | ROW emis | EMEP region emis | $CH_4$ (ppb) |
|---|---|---|---|---|
| Baseline 2015 | bs15_bs15ch4 | 2015 baseline | 2015 baseline | 1834 |
| Baseline 2015 to ROW 2050 CLE emis | rowcle50_bs15ch4 | 2050 CLE | 2015 baseline | 1834 |
| Baseline 2015 to global 2050 CLE emis | cle50_bs15ch4 | 2050 CLE | 2050 CLE | 1834 |
| Global 2050 CLE | cle50_cle50ch4 | 2050 CLE | 2050 CLE | 2236 |
| 2050 CLE to ROW 2050 MFR emis | rowmfr50_cle50ch4 | 2050 MFR | 2050 CLE | 2236 |
| 2050 CLE to global 2050 MFR emis | mfr50_cle50ch4 | 2050 MFR | 2050 MFR | 2236 |
| Global 2050 MFR | mfr50_mfr50ch4 | 2050 MFR | 2050 MFR | 1651 |
| 2050 MFR to ROW 2050 LOW emis | rowlow50_mfr50ch4 | 2050 LOW | 2050 MFR | 1651 |
| 2050 MFR to global 2050 LOW emis | low50_mfr50ch4 | 2050 LOW | 2050 LOW | 1651 |
| Global 2050 LOW | low50_low50ch4 | 2050 LOW | 2050 LOW | 1574 |

$$CH_4(\phi, CH_4{}^*) = CH_4{}^* \left( 1 + \frac{0.025\phi}{90} \right), \tag{1}$$

250 where $CH_4{}^*$ represents the global mean background concentration and $\phi$ is latitude in degrees. For pre-industrial (808 ppb) and the year 2015 (1834 ppb) global mean $CH_4$ concentrations, Eq. 1 yields latitudinal gradients of 40 ppb and 92 ppb, respectively, consistent with those described in Meinshausen et al. (2017). By applying Eq. 1 also for the projected $CH_4$ concentrations, an approach similar to that of Meinshausen et al. (2020) is followed, by effectively using EOF1 to extrapolate the latitudinal gradient into the future based on anthropogenic $CH_4$ emissions.

255 **4.2 Scenario configurations**

To simulate the effects of precursor emission changes inside and outside of the EMEP region, regional simulations are combined with LBCs from the global model configuration. Simulations where only background $CH_4$ concentrations are changed serve to isolate the impact of global $CH_4$ change. Since $CH_4$ is a globally well-mixed gas, and since the concentration changes are the result of anthropogenic $CH_4$ emission changes, the impact of the total global mean $CH_4$ change is split into its EMEP region 260 and ROW contributions based on the $CH_4$ emission changes within these respective regions. This approach is supported by the surface $O_3$ response being effectively linear in the range of $CH_4$ concentrations relevant to the current work, as discussed in Sect. 6.1. An overview of the scenario simulations is shown in Table 2, noting that each of the configurations is simulated for each of the five meteorological years between 2013-2017 for both the regional and global setups, as discussed in the following.

## 4.3 Baseline evaluation against observation

265 The efficacy of the EMEP model to simulate peak season MDA8 is evaluated by comparing the baseline configuration to surface observations. To this end, the baseline 2015 configuration is used to perform simulations for the 2013-2017 meteorological years, and compared against surface observations from the EBAS database (Laj et al., 2024; Tørseth et al., 2012). While the anthropogenic emissions are fixed to that of the year 2015, inter-annual variability in the emissions is generally small. The 56 EBAS stations are located within the European part of the EMEP region (as shown in supplementary Fig. S2), and are

270 selected from all available stations based on the requirement that they each measure peak season MDA8 for each of the five meteorological years. For MDA8, data availability guidelines stipulate that for each 8-hourly mean 75% of the hourly values must be present, while at least 75% of the eight hour averages must be present in a day to assign a maximum daily 8-hour mean (EU, 2008). Data availability guidelines similar to those for annual mean $O_3$ are also adopted, requiring that at least 90 % of the days between April-September have MDA8 measurements available to assign a peak season average. We note that the data

275 availability requirements have no significant impact on the geographical spread or conclusions of the model to measurement comparison.

Fig. 2a compares the five-year average modelled and observed peak season MDA8 values at each of the 56 stations. A clear relationship between the modelled and observed values is present, having a Pearson correlation coefficient (r) of 0.87. The normalized mean bias (NMB) amounts to 3.7 %, indicating that the model has a slight tendency to overestimate. Fig. 2b shows

280 the annual averages across all 56 stations, illustrating that the total inter-annual variability for both model and measurements corresponds to around 4-5 µg m$^{-3}$. The difference between the total annual average modelled and observed concentrations is greatest for the year 2014, amounting to 6.4 µg m$^{-3}$ (7.6 %), while being as low as 0.1 µg m$^{-3}$ (0.1 %) for the year 2013. The difference in the five-year average measured (84.6 µg m$^{-3}$) and modelled (87.8 µg m$^{-3}$) concentrations follows that of the NMB (3.2 µg m$^{-3}$, or 3.7 %). In Fig. 2c, annual averages across all stations within Sweden, Germany, Spain, the United

285 Kingdom, and Poland are shown, illustrating that the model generally captures the observed variability between high and low $O_3$ years also at regional scales. Observed concentrations in these countries were the lowest in 2017, except for in Spain, as also reproduced by the model. The observed differences between the highest (2015) and lowest year (2017) can be as large as 13.3 µg m$^{-3}$ (17.7 %), for example for Poland. The modelled inter-annual variability in the different regions is approximately equal to, or sometimes smaller than (e.g., Poland, Spain), the observed variability. For Poland, the difference between the

290 highest and lowest modelled year amounts to 7.5 µg m$^{-3}$ (8.5 %), being lower by 5.8 µg m$^{-3}$ than the observed maximum variability.

Overall, the EMEP model displays generally good agreement with observations across the five meteorological years, while highlighting that inter-annual peak season MDA8 variability can be on the order of 10-15 % on regional scales and around 5 % across Europe. To reduce the effects of meteorological variability, each of the scenarios listed in Table 2 is therefore simulated

295 for the years 2013-2017, with the results presented in the following representing five-year averages.
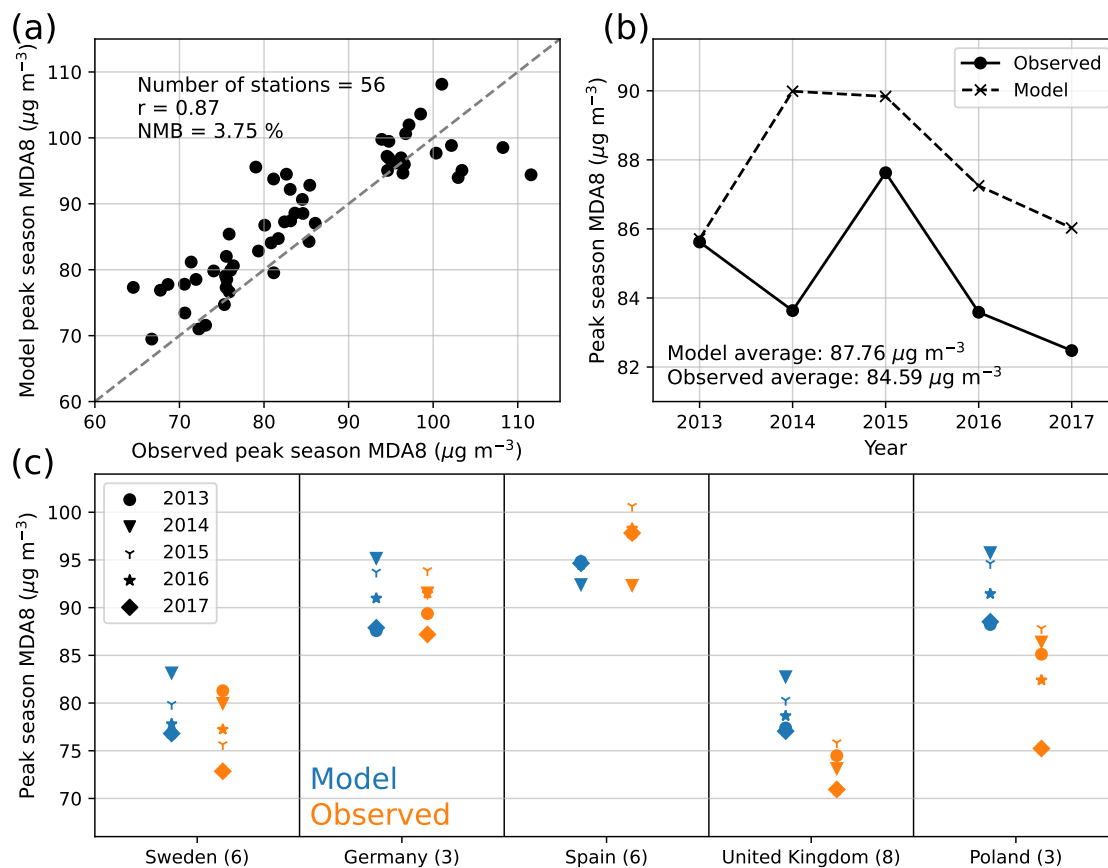
**Figure 2.** Modelled versus observed peak season MDA8 across Europe. Panel (a) shows five-year averaged values at each of the 56 stations, while panel (b) compares the annual values averaged over all stations. Panel (c) shows the yearly averages for Sweden, Germany, Spain, the United Kingdom, and Poland, with the number in brackets indicating the number of stations in each of the countries.

## 5 Results

While the focus in this section lies on peak season MDA8, results for other $O_3$ indicators are included in the supplementary material, as referred to in the text. In addition, the following discusses a number of weighted averaging approaches for both health and vegetation $O_3$ indicators, with the different population and crop-area maps shown for reference in supplementary Fig. S3.

### 5.1 EMEP region peak season MDA8

Fig. 3 shows a so-called cascade-plot of the EMEP region population weighted peak season MDA8 changes between the 2015 baseline and the 2050 CLE, MFR, and LOW scenarios. Here the population weighting is calculated using the Global Human Settlement Layer (GHSL) population distribution for the year 2015 (Schiavina et al., 2023), aggregated from its native 3 arc-second resolution to the regional EMEP grid, remaining unchanged for all scenarios. In Fig. 3, the impacts arising from $NO_x$, CO, and NMVOC precursor emissions changes and from $CH_4$ are shown as separate cascade-steps. In the cascades, the separate contributions arising from EMEP region and ROW emission changes are also highlighted, as calculated using the model configurations described in Table 2. For example, the difference between the 'bs15_bs15ch4' and 'rowcle50_bs15ch4' simulations yields the change due to 2050 CLE precursor emission changes in the ROW region relative to the 2015 baseline, whereas the difference between the 'cle50_bs15ch4' and 'cle50_cle50ch4' simulations yields the change due to background $CH_4$ changes. The direction of the changes (increasing or decreasing) is illustrated using red arrows for the 2015 baseline to 2050 CLE scenario, highlighting that in this case increasing $CH_4$ concentrations lead to an increase in peak season MDA8. As noted in Sect 4, the impact of global $CH_4$ emission changes is split into its EMEP and ROW region contributions based on the emission changes within these respective regions. In effect, the cascade-plot thereby summarizes the impact of each of successive precursor and $CH_4$ change from the 2015 baseline down to the 2050 LOW scenario.

Fig. 3 shows that average peak season MDA8 concentrations are reduced from 91.8 to 89.2 µg m$^{-3}$ between the 2015 baseline and 2050 CLE scenarios, resulting largely from a decrease in precursor emissions in the EMEP region (-4.5 µg m$^{-3}$) and to a lesser extent in the ROW region (-1.4 µg m$^{-3}$). However, these reductions are partially offset by an increase of 3.2 µg m$^{-3}$ arising from increased background $CH_4$ concentrations, being almost entirely the result of increased $CH_4$ emissions in the ROW region. Going from the 2050 CLE to 2050 MFR scenario, the net reduction from 89.2 to 75.4 µg m$^{-3}$ (-15.4 %) is split into three nearly equal parts arising from EMEP region precursor reductions, ROW precursor reductions, and background $CH_4$ reductions. The 2050 LOW scenario differs relatively little from the MFR, with roughly half of the change from 75.4 to 72.2 µg m$^{-3}$ arising from further precursor emission reductions within the EMEP region. Cascade-plots for the annual $O_3$ mean, SOMO35, and POD$_3$IAM$_{WH}$ indicators, as discussed in Sect. 5.2, are shown in supplementary Fig. S4-S6.

### 5.1.1 Geographical distribution

To illustrate the impact of geographical location on the $O_3$ changes resulting from precursor and $CH_4$ emission changes, the difference in peak season MDA8 between the 2050 CLE and LOW scenarios is shown across the regional EMEP modelling

16
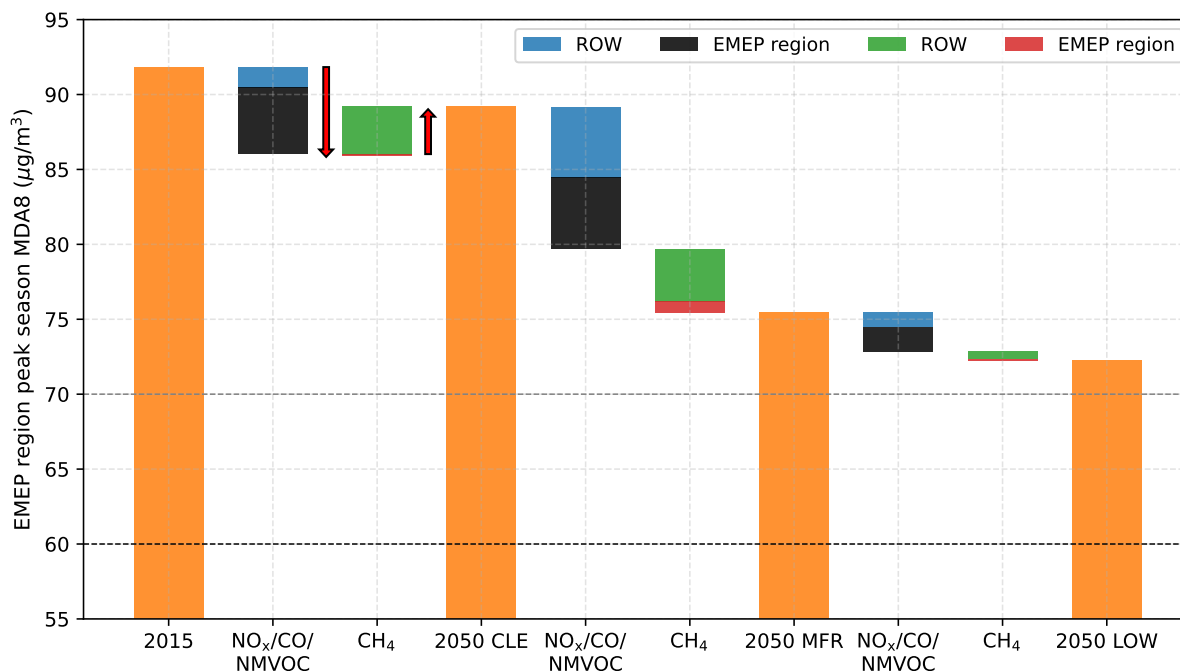
**Figure 3.** Cascade plot of the population weighted EMEP region average peak season MDA8 scenario changes arising from $NO_x$, CO, and NMVOC emission changes within the EMEP (black) and ROW (blue) regions, and from background $CH_4$ changes arising from EMEP (red) and ROW (green) region emission changes. The black and grey dashed horizontal line denote guideline and interim WHO target values, respectively. Red arrows indicate the direction of the cascades from the 2015 baseline to 2050 CLE scenario for illustration, as described in the text.

domain in Fig. 4. Here the 2050 CLE to LOW impacts are calculated by combining the results from the 2050 CLE to 2050 MFR simulations with the 2050 MFR to 2050 LOW simulations described in Table 2. Fig. 4a shows the change in peak season MDA8

330    resulting from the change to ROW LOW emissions. As expected, the ROW LOW impacts are most pronounced in the ROW countries within the regional modelling domain (e.g., North African countries). Nevertheless, countries along the Southern border of the EMEP region as well as along the Western coast of Europe also see reductions ranging from 5-15 µg m$^{-3}$. The reductions along the Western coast of Europe are likely the result of emission reductions in North America, with the associated $O_3$ perturbations carried over the Atlantic ocean by the prevailing Westerlies. Fig. 4b shows that the impact of regional LOW

335    emissions is largely centered on the EMEP region, ranging from approximately 5 µg m$^{-3}$ in Western Europe to 30 µg m$^{-3}$ in West-Balkan and EECCA countries. While local in nature, the impact of emission reductions in both the EMEP and ROW regions can lead to increases of as much as 30 µg m$^{-3}$ in large urban areas (as highlighted in Fig. 4b for Almaty, Kazakhstan), due to reductions in the titration effect of $NO_x$. The impact of background $CH_4$ reductions from 2236 to 1574 ppb is shown in Fig. 4c, with the latitudinal gradient likely to a large extent arising from the latitudinal variations in insolation. The resulting

340    peak season MDA8 reductions amount to around 5 µg m$^{-3}$ across the EMEP region.

**17**
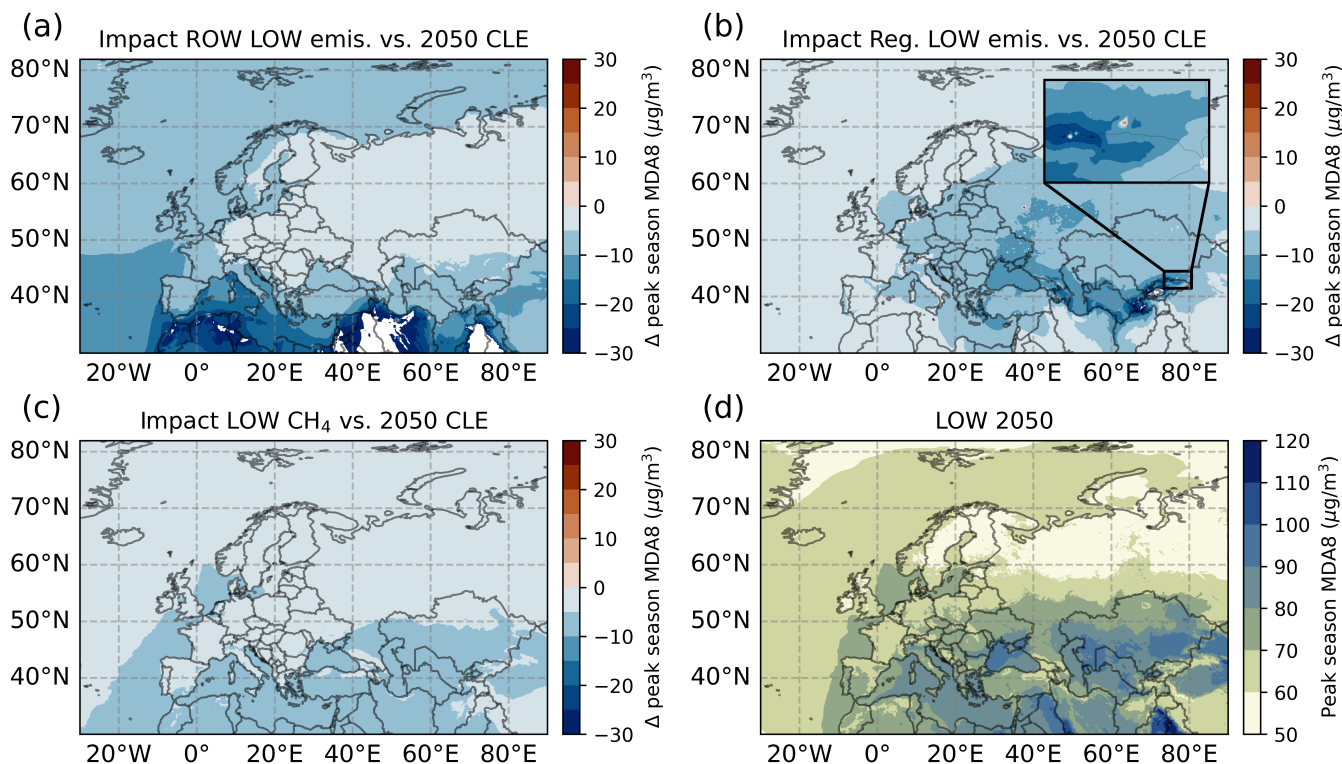
**Figure 4.** Reductions in peak season MDA8 achieved by 2050 ROW LOW (panel a) and EMEP region (panel b) precursor emission changes relative to the 2050 CLE scenario. Panel (b) also highlights the simulation results for Almaty, Kazakhstan. Panel (c) shows the reductions arising from the background $CH_4$ change from 2236 to 1574 ppb, while panel (d) shows the peak season MDA8 as simulated for the full 2050 LOW scenario. Note the difference in color-scale for panel (d).

Fig. 4d shows the results for the full 2050 LOW scenario, illustrating that peak season MDA8 concentrations fall below 60 µg m$^{-3}$ over parts of northern Scandinavia, while ranging from 80 to 90 µg m$^{-3}$ over Northern Italy and Kazakhstan. In Central Europe, concentrations typically range from 60-70 µg m$^{-3}$, highlighting that the population weighted WHO exposure guideline of 60 µg m$^{-3}$ is, in fact, not met in any of the EMEP countries. However, the interim target of 70 µg m$^{-3}$ is reached in a number of Western European countries, such as the Netherlands, France, Germany, and the United Kingdom. The population weighted LOW scenario concentrations for each of the individual countries in the EMEP region are shown in supplementary Fig. S7, along with their 2015 baseline and 2050 CLE and MFR concentrations. In addition, supplementary Fig. S8 follows that of Fig. 4, but instead compares the impacts of the LOW scenario against the 2015 baseline. For the latter, the impact of regional emission reductions is comparatively higher, while that of $CH_4$ changes is comparatively lower, consistent with the results shown in Fig. 3.

## 5.2 Other $O_3$ indicators

This section serves in part to provide reference to earlier studies by showing the scenario results for a range of other health and vegetation $O_3$ indicators. For example, earlier works have investigated the impact of precursor and $CH_4$ emission changes on (area weighted) annual mean surface $O_3$ ("$O_3$ mean") concentrations (Turnock et al., 2018; Jonson et al., 2018), while the Sum of Ozone Means Over 35 ppb (SOMO35), 4th highest annual MDA8, and summertime (JJA) average daily maximum $O_3$ concentrations have been used for health impact studies (Fleming et al., 2018). Furthermore, JJA average $O_3$ concentrations were used in the study of the climate-impact on surface $O_3$ by Colette et al. (2015), as will be discussed in more detail in Sect. 6. For the impacts on vegetation, the growing-season accumulated Phyto-toxic Ozone Dose ($POD_Y$) uptake over a certain threshold value $Y$ (nmole $O_3$ m$^{-2}$ s$^{-1}$) can induce reductions in crop and semi-natural biomass (Emberson, 2020; Mills et al., 2018). To this end, the Integrated Assessment Modelling (IAM) vegetation-type specific $POD_Y$ indicators ($POD_Y$IAM) serve as simplified risk assessment indicators for use in CTMs such as the EMEP model (Simpson et al., 2012, 2007), as also described in the UNECE 'Mapping Manual' (UNECE, 2017). The $POD_3IAM_{WH}$ indicator represents the cumulative growing-season ($\sim$90 days) stomatal $O_3$ uptake for a generic temperate or boreal crop, being largely based on wheat (WH), and is used as an indicator for wheat yield loss (Pandey et al., 2023; Mills et al., 2018). In addition, the $POD_1IAM_{DF}$ indicator is used in the risk assessment of reductions in annual living deciduous forest (DF) biomass growth (UNECE, 2017), having a $\sim$180 day growing season at 50°N.

Table 3 shows the absolute and percentage change scenario results across the range of $O_3$ indicators for an extended range of (constructed) scenarios. For example, the '2015 Base to 2050 MFR' scenario is constructed using the differences between the '2015 Base to 2050 CLE' and the '2050 CLE to 2050 MFR' scenarios described in Table 2, while the '2050 CLE to 2050 LOW' scenario is constructed using the differences between the '2050 CLE to 2050 MFR' and '2050 MFR to 2050 LOW' scenarios (as described in Sect. 5.1.1). Likewise, the '2015 Base to 2050 LOW' scenario is constructed using the differences between the '2015 Base to 2050 CLE', '2050 CLE to 2050 MFR', and '2050 MFR to 2050 LOW' scenarios. Note that for peak season MDA8, the absolute numbers shown for the '2015 Base to 2050 CLE', '2050 CLE to 2050 MFR', and '2050 MFR to 2050 LOW' scenarios correspond to those shown in Fig. 3. Furthermore, since the relative importance of $CH_4$ emission changes inside the EMEP region is small, Table 3 only includes the impact of global $CH_4$ changes. While health-related $O_3$ indicators are shown as population weighted averages, the $POD_Y$ indicators are shown as their respective vegetation-area weighted averages (i.e., average values per square meter of vegetation, as illustrated in supplementary Fig. S3).

Table 3 illustrates that different uses of threshold values and time and length of averaging or accumulation periods leads to differences in the relative importance of precursor and $CH_4$ emission changes. For example, indicators most sensitive to $O_3$ concentrations during its peak photochemical production period (peak season MDA8, JJA $O_3$ max, JJA $O_3$ mean, and 4th highest MDA8) are most strongly impacted by regional precursor emission reductions, especially when compared against the 2015 baseline scenario. In contrast, regional emission reductions are much less important for annual $O_3$, due to the competing effects of local wintertime $NO_x$ titration. The importance of ROW emissions is, broadly speaking, proportional to the length of the averaging or accumulation period, while also being most relevant to the 2050 scenarios (i.e., 2050 CLE

**Table 3.** Absolute and percentage change (in brackets) scenario impacts across the EMEP region. Changes resulting from precursor emission changes in the EMEP (reg.) and ROW regions, and from global $CH_4$ changes, are shown relative to the scenario starting points. End values correspond to the weighted averages at each of the scenario end-points.

| Scenario | | 2015 Base to 2050 CLE | 2015 Base to 2050 MFR | 2015 Base to 2050 LOW | 2050 CLE to 2050 MFR | 2050 CLE to 2050 LOW | 2050 MFR to 2050 LOW |
|---|---|---|---|---|---|---|---|
| PS MDA8[a] | Reg. emis | -4.5 (-4.9 %) | -9.3 (-10.1 %) | -10.9 (-11.9 %) | -4.8 (-5.4 %) | -6.4 (-7.2 %) | -1.6 (-2.2 %) |
| | ROW emis | -1.4 (-1.5 %) | -6.0 (-6.6 %) | -7.0 (-7.6 %) | -4.7 (-5.2 %) | -5.7 (-6.3 %) | -1.0 (-1.3 %) |
| | $CH_4$ | 3.1 (3.4 %) | -1.1 (-1.2 %) | -1.7 (-1.8 %) | -4.2 (-4.8 %) | -4.8 (-5.4 %) | -0.6 (-0.8 %) |
| | End value | 89.2 | 75.4 | 72.2 | 75.4 | 72.2 | 72.2 |
| $O_3$ mean[a] | Reg. emis | 1.2 (2.0 %) | 0.3 (0.4 %) | -0.3 (-0.5 %) | -1.0 (-1.5 %) | -1.5 (-2.4 %) | -0.6 (-1.0 %) |
| | ROW emis | -1.0 (-1.7 %) | -5.2 (-8.6 %) | -6.1 (-10.0 %) | -4.2 (-6.6 %) | -5.1 (-8.0 %) | -0.9 (-1.6 %) |
| | $CH_4$ | 2.1 (3.5 %) | -0.8 (-1.3 %) | -1.2 (-2.0 %) | -2.9 (-4.6 %) | -3.3 (-5.3 %) | -0.4 (-0.7 %) |
| | End value | 63.5 | 55.4 | 53.5 | 55.4 | 53.5 | 53.5 |
| 4th MDA8[a] | Reg. emis | -9.0 (-6.2 %) | -15.8 (-11.0 %) | -18.2 (-12.6 %) | -6.8 (-5.0 %) | -9.2 (-6.7 %) | -2.4 (-2.0 %) |
| | ROW emis | -1.0 (-0.7 %) | -4.8 (-3.3 %) | -5.7 (-3.9 %) | -3.8 (-2.8 %) | -4.7 (-3.4 %) | -0.9 (-0.7 %) |
| | $CH_4$ | 3.2 (2.2 %) | -1.0 (-0.7 %) | -1.5 (-1.1 %) | -4.2 (-3.1 %) | -4.8 (-3.5 %) | -0.6 (-0.5 %) |
| | End value | 137.5 | 122.7 | 118.9 | 122.7 | 118.9 | 118.9 |
| JJA $O_3$ max[d] | Reg. emis | -7.0 (-6.8 %) | -13.8 (-13.3 %) | -16.0 (-15.5 %) | -6.8 (-6.8 %) | -9.0 (-9.1 %) | -2.2 (-2.7 %) |
| | ROW emis | -1.2 (-1.1 %) | -5.2 (-5.0 %) | -5.9 (-5.7 %) | -4.0 (-4.0 %) | -4.7 (-4.7 %) | -0.7 (-0.8 %) |
| | $CH_4$ | 3.8 (3.6 %) | -1.2 (-1.2 %) | -1.9 (-1.8 %) | -5.0 (-5.0 %) | -5.7 (-5.7 %) | -0.7 (-0.8 %) |
| | End value | 99.0 | 83.2 | 79.6 | 83.2 | 79.6 | 79.6 |
| JJA $O_3$ mean[a] | Reg. emis | -3.3 (-4.6 %) | -6.4 (-8.8 %) | -7.5 (-10.4 %) | -3.0 (-4.2 %) | -4.2 (-5.9 %) | -1.2 (-1.9 %) |
| | ROW emis | -0.9 (-1.3 %) | -4.3 (-6.0 %) | -4.9 (-6.8 %) | -3.4 (-4.8 %) | -4.0 (-5.7 %) | -0.6 (-1.0 %) |
| | $CH_4$ | 2.9 (4.0 %) | -1.0 (-1.4 %) | -1.6 (-2.2 %) | -3.9 (-5.5 %) | -4.4 (-6.3 %) | -0.5 (-0.9 %) |
| | End value | 70.8 | 60.5 | 58.2 | 60.5 | 58.2 | 58.2 |
| SOMO35[b] | Reg. emis | -390 (-12.7 %) | -904 (-29.5 %) | -1043 (-34.1 %) | -514 (-18.0 %) | -653 (-22.8 %) | -139 (-10.4 %) |
| | ROW emis | -158 (-5.2 %) | -787 (-25.7 %) | -893 (-29.2 %) | -628 (-21.9 %) | -734 (-25.7 %) | -106 (-8.0 %) |
| | $CH_4$ | 347 (11.3 %) | -35 (-1.2 %) | -79 (-2.6 %) | -383 (-13.4 %) | -427 (-14.9 %) | -43 (-3.3 %) |
| | End value | 2863 | 1337 | 1047 | 1337 | 1047 | 1047 |
| POD$_3$IAM$_{WH}$[c] | Reg. emis | -1.5 (-9.9 %) | -2.7 (-17.5 %) | -3.1 (-20.0 %) | -1.2 (-8.1 %) | -1.6 (-10.8 %) | -0.4 (-3.7 %) |
| | ROW emis | -0.4 (-2.5 %) | -1.8 (-11.5 %) | -2.0 (-13.0 %) | -1.4 (-9.6 %) | -1.6 (-11.2 %) | -0.2 (-2.3 %) |
| | $CH_4$ | 0.9 (6.0 %) | -0.3 (-2.0 %) | -0.5 (-3.1 %) | -1.2 (-8.5 %) | -1.4 (-9.7 %) | -0.2 (-1.6 %) |
| | End value | 14.5 | 10.7 | 9.9 | 10.7 | 9.9 | 9.9 |
| POD$_1$IAM$_{DF}$[c] | Reg. emis | -2.3 (-10.1 %) | -4.2 (-18.1 %) | -4.8 (-20.6 %) | -1.9 (-8.8 %) | -2.5 (-11.5 %) | -0.6 (-3.4 %) |
| | ROW emis | -0.5 (-2.1 %) | -1.8 (-7.8 %) | -2.1 (-9.0 %) | -1.3 (-6.2 %) | -1.6 (-7.4 %) | -0.3 (-1.5 %) |
| | $CH_4$ | 1.0 (4.2 %) | -0.4 (-1.5 %) | -0.5 (-2.3 %) | -1.3 (-6.2 %) | -1.5 (-7.0 %) | -0.2 (-1.1 %) |
| | End value | 21.3 | 16.8 | 15.8 | 16.8 | 15.8 | 15.8 |

[a]Population weighted EMEP region average in µg m$^{-3}$. [b]Population weighted EMEP region average in ppb day$^{-1}$. [c]Crop-area weighted EMEP region average in mmol m$^{-2}$.
[d]Population weighted average converted from ppb to µg m$^{-3}$ using the standard-atmosphere $O_3$ conversion factor of 1.96.

385 to MFR and LOW). For indicators employing a threshold value, the percentage-change impacts are proportional to the height of the threshold relative to the baseline (or background) value, which effectively determines the degree to which the natural background is filtered out. For example, the total percentage-change reduction from the 2015 baseline to 2050 LOW scenarios for the SOMO35, $POD_3IAM_{WH}$, and $POD_1IAM_{DF}$ indicators amounts to 65.8 %, 40.3 %, and 31.9 %, respectively. While already implied in Fig. 3, Table 3 also shows that the impact of $CH_4$ emission reductions is most important relative to the 2050

390 CLE scenario, and less so when compared against the 2015 baseline. However, $O_3$ mean is an exception to the latter, with $CH_4$ having the largest impact from the 2015 baseline to 2050 CLE scenario. Furthermore, $CH_4$ reductions contribute roughly one thirds of the total reductions for each of the peak $O_3$ indicators for the 2050 CLE to 2050 MFR scenario, although this is closer to one-fourths for SOMO35 (25.1 %).

For the population weighted $O_3$ indicators (i.e., all except those for vegetation), the corresponding area weighted averages are

395 shown in supplementary Table S2. While the results are generally consistent between the two weighted averaging approaches, indicators sensitive to peak $O_3$ concentrations are comparatively less impacted by regional precursor emission changes when calculated as area weighted averages. However, the area weighted impacts of regional precursor emission changes are considerably larger for annual $O_3$ mean, since $NO_x$ titration effects in urban areas are weighted less heavily. For example, reducing regional emissions between the 2015 baseline to 2050 MFR scenarios sees a population weighted $O_3$ mean reduction of

400 0.3 µg m$^{-3}$ (0.4 %), while the corresponding area weighted reduction amounts to 5.1 µg m$^{-3}$ (7.7 %).

## 6    Discussion

In the current setup, the EMEP model is unable to capture the effects of future climate change on surface $O_3$ concentrations. This effect, often described as the $O_3$ climate penalty (e.g., Fu and Tian, 2019; Rasmussen et al., 2013), can affect surface $O_3$ for example through climate-change induced changes in water vapour concentrations and biogenic VOC emissions. For European land surfaces, Colette et al. (2015) estimated the 95 % confidence interval of the mid-century (2041-2070) surface JJA $O_3$ mean climate penalty to range from 0.44-0.64 ppb, based on an ensemble of 25 chemistry-climate model simulations. Compared to the JJA $O_3$ mean changes between the 2050 CLE and MFR scenarios shown in Table 3, amounting to 10.3 µg m$^{-3}$ (or 5.2 ppb using the standard-atmosphere $O_3$ conversion factor of 1.96), the impact of the climate penalty on the results of the current work is expected to be small. Other climate-uncertainties relate to the calculated $CH_4$ projections, with terrestrial soil emissions estimated to increase by $22.8 \pm 3.6$ Tg $CH_4$ yr$^{-1}$ by the year 2100 in the SSP5-8.5 scenario (Guo et al., 2023). However, by the year 2050 and relative to the baseline natural emissions, estimated at 210 Tg yr$^{-1}$ in Sect. 3, the change in natural emissions is expected to be comparatively small, and in part captured by increasing permafrost emissions as described in Sect. 3.

While constructing emission data sets based on a wide variety of information is by itself challenging (e.g., de Meij et al., 2024; Thunis et al., 2022), the emission scenarios employed in the current work are also inherently based on a number of socio-economic activity projections. In practice, the reliable quantification of the uncertainty on the input parameters to the GAINS model is itself considered the most uncertain element of the analysis (Amann et al., 2011). In light of this, the emission scenarios arguably represent the largest source of uncertainty in the current work, which is unavoidable and not directly quantifiable. Nevertheless, the GAINS model by design attempts to minimize the impact of uncertainties on policy-relevant model output, to increase the robustness (i.e., the priorities and control needs between countries, sectors and pollutants do not significantly change due to uncertainties in the model elements) of the emission control strategies (Amann et al., 2011).

### 6.1    $O_3$ production efficiency of $CH_4$

The $CH_4$ oxidation reaction that leads the production of $O_3$ depends on the availability of $NO_x$ and OH (Crutzen et al., 1999). OH is produced through the photolysis of $O_3$ and subsequent reaction of $O(1D)$ with water vapour ($H_2O$), with the majority of surface $O_3$ being produced by the photolysis of $NO_x$ in VOC-rich environments. In addition, CO and VOCs (including $CH_4$) are net sinks of OH, creating a non-linear relationship between their atmospheric abundance and the $O_3$ production efficiency (OPE) of $CH_4$ (Isaksen et al., 2014). In the current work, the OPE is taken as the capacity of $CH_4$ to produce surface $O_3$ in the EMEP region. To investigate the impact of OPE on the calculated $O_3$ response, diagnostic EMEP model simulations are performed where background $CH_4$ concentrations are varied between 850 to 2600 ppb in 250 ppb steps, using both the 2015 baseline and the 2050 CLE and LOW emission scenarios as the source of background precursor emissions. The resulting $CH_4$ impacts on peak season MDA8 are shown in Fig. 5, noting that the starting point of 850 ppb corresponds roughly to pre-industrial $CH_4$ concentrations. For simplicity, the simulations shown here are only calculated for the 2015 meteorological year, but with otherwise the same model configuration (e.g., six month spin-up period) as described in Sect. 4.
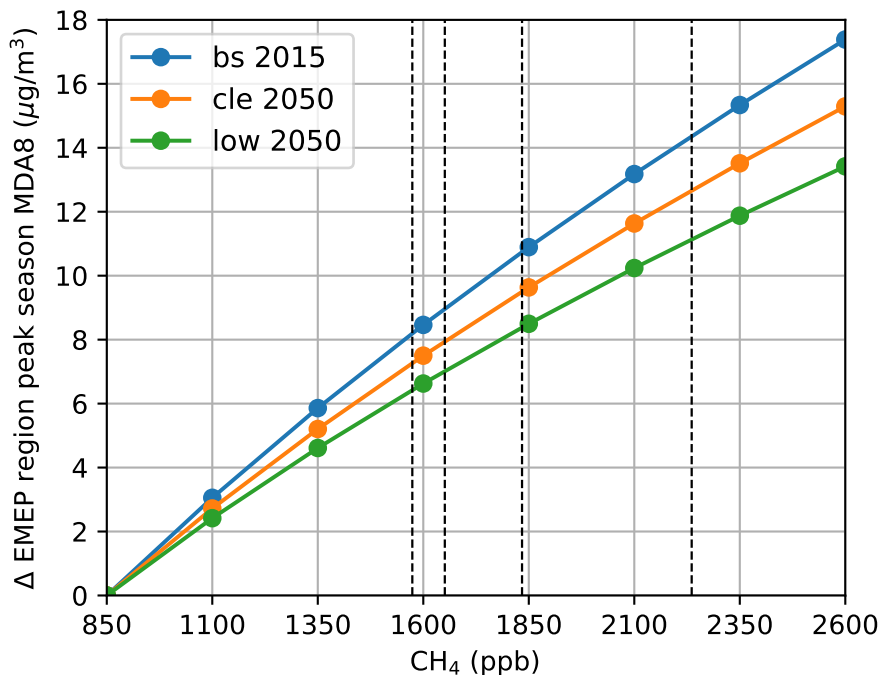
**Figure 5.** Change in EMEP region population weighted peak season MDA8 for background $CH_4$ concentrations ranging from 850 to 2600 ppb in 250 ppb intervals, relative to peak season MDA8 concentrations at 850 ppb $CH_4$. The impacts are calculated with the baseline 2015 and the 2050 CLE and LOW emission scenarios defined in Table 2. The dashed vertical lines mark the 2050 LOW, 2050 MFR, 2015 baseline, and 2050 CLE background $CH_4$ concentrations (1574, 1651, 1834, and 2236 ppb, respectively) as discussed in Sect. 3.

Fig. 5 illustrates that the OPE is highest in the 2015 baseline scenario, when EMEP region $NO_x$ emissions are also highest
435 (Table 1). Regional $NO_x$ emissions are reduced considerably already in the 2050 CLE scenario, while other emissions change relatively little. As a result, the OPE is a factor of 0.88 (12 %) smaller relative to the 2015 baseline across the range of $CH_4$ concentrations. Similarly, the OPE in the 2050 LOW scenario is a factor of 0.88 (12 %) lower than that of the 2050 CLE scenario, and by a factor of 0.78 (22 %) relative to the 2015 baseline scenario. The decrease from 2236 to 1574 ppb $CH_4$ between the 2050 CLE to 2050 LOW scenarios discussed in Sect. 3 leads to a reduction of peak season MDA8 by 5.4 and 4.7
440 $\mu g\ m^{-3}$ when calculated with CLE and LOW precursor emissions, respectively. The reduction of 4.9 $\mu g\ m^{-3}$ due to $CH_4$ as shown in Table 3, being calculated with a combination of 2050 MFR and 2050 LOW precursor emissions, therefore depends relatively little on the choice of background precursor emissions and more so on the background $CH_4$ changes itself.

Fig. 5 furthermore illustrates that the peak season MDA8 response is approximately linear in the range of $CH_4$ concentrations relevant to the current work, supporting the approach of splitting the $O_3$ impacts based on the separate emission changes within
445 the EMEP and ROW regions. Another corollary is that the contribution of anthropogenic background $CH_4$ to total peak season MDA8 can be calculated to amount to approximately 10.7 (11.6 %), 12.7 (14.2 %), and 6.4 (8.9 %) $\mu g\ m^{-3}$ in the 2015

baseline, 2050 CLE, and 2050 LOW scenarios, respectively. Here the percentage contributions are based on the scenario totals shown in Fig. 3 and Table 3. Recognizing that the MFR and LOW precursor emission scenarios are nearly identical except for $CH_4$ emissions, the anthropogenic $CH_4$ contribution calculated for the 2050 MFR scenario (1651 ppb) amounts to 7.0 µg m$^{-3}$ (9.3 %).

## 6.2 Comparison to previous studies

While important for placing the results in context, comparing the results of the current work to earlier studies can be challenging, for example due to differences in source-receptor area definitions, model configuration, weighted averaging approach, and emission scenarios. Nevertheless, while the modeling setup of Belis and Van Dingenen (2023) is different in that linear pre-calculated transfer coefficients of the TM5-FAst Scenario Screening Tool (TM5-FASST) are used in place of full CTM simulations, our calculated EMEP region total peak season MDA8 exposure reduction by 15 % between the 2050 CLE and MFR scenarios is consistent with their 16 % reduction found across the entire UNECE region (including North America) based on CLE and MFR scenarios from the ECLIPSE version 6b dataset. However, in our calculations the total 2050 MFR anthropogenic $CH_4$ contribution amounts to 7.0 µg m$^{-3}$ (or 3.5 ppb using the standard-atmosphere $O_3$ conversion factor of 1.96), which is lower than their estimate of $\sim$ 5 ppb (based on their Fig. S4). This can largely be reconciled considering that our estimate was calculated with the 2050 LOW scenario as the source of background precursor emissions, while theirs is based on $O_3$ sensitivities calculated from a 2010 baseline emission scenario. When using the 2015 baseline emission scenario as the source of background precursor emissions in our calculations, the total 2050 MFR anthropogenic $CH_4$ contribution amounts to 9.0 µg m$^{-3}$, or 4.5 ppb, which is more comparable.

In the work of Turnock et al. (2018), the box-model described in Holmes et al. (2013) is used to estimate the 2050 CLE and MFR $CH_4$ concentrations to amount to 2361 and 1420 ppb, respectively. They further estimate the 2050 CLE increase in $CH_4$ to contribute 1.6 ppb to annual mean area weighted $O_3$ across Europe relative to a 2010 baseline concentration of 1798 ppb, based on the parameterized response of 14 models. While the latter is higher than our estimate of 1.1 ppb for the EMEP region (Table S3, using the standard-atmosphere $O_3$ conversion factor of 1.96), our results find a more comparable contribution of 1.4 ppb when the response is calculated as the European area weighted average following the land-area definition of Turnock et al. (2018). However, in our results the 2050 CLE and MFR ensemble mean $CH_4$ concentrations amount to 2236 and 1651 ppb, respectively, with the total difference between the CLE and MFR scenarios therefore being 403 ppb (or 43 %) less than that of Turnock et al. (2018). While this may in part be due to their MFR scenario diverging from the CLE from 2020 rather than 2025 onwards, it nevertheless highlights the importance of the methodology used to estimate $CH_4$ concentrations, as the cumulative difference between scenarios can quickly diverge. The difference in $CH_4$ estimates also has implications for the impact of the 2050 MFR emissions relative to the baseline, which in our analysis (-183 ppb) is around half that determined by Turnock et al. (2018) (-378 ppb).

## 6.3 Air-pollution and global warming co-benefits

While a detailed discussion is beyond the scope of the current work, the global mean temperature change relative to the reference period of 1986-2005, as calculated for the 600-ensemble mean and 5-95 % range using the MAGICC7 model in Sect. 3, amounts to 2.21 [1.61-2.94], 2.02 [1.45-2.74], and 1.92 [1.33-2.67] degrees K for the 2050 CLE, MFR, and LOW scenarios, respectively. In the LOW-$CH_4$ scenario, where $CH_4$ emissions follow the LOW scenario while all other emissions follow that of the CLE, this change amounts to 2.03 [1.47-2.74] degrees K. Thus illustrating that around two-thirds of the global warming reduction between the 2050 CLE (SSP2-4.5 GHGs) and LOW (SSP1-2.6 GHGs) scenarios can be achieved by solely reducing $CH_4$ emissions.

25

## 7 Conclusion

This work investigates the impact of $CH_4$ and other precursor emissions on surface $O_3$ concentrations in the EMEP region for the CLE, MFR, and LOW emission scenarios up to the year 2050. In the CLE scenario, background $CH_4$ concentrations are projected to increase by 402 ppb (22 %) relative to 2015 baseline concentrations, while they are reduced by 183 ppb (-10 %) in the MFR scenario. By 2050, the difference between the MFR and CLE scenarios therefore amounts to 585 ppb (or 26.1 % less in the MFR compared to the CLE), while the LOW scenario achieves a modest further 77 ppb reduction. The MFR $CH_4$ reductions lead to a peak season MDA8 exposure reduction of 4.2 µg m$^{-3}$ (4.8 %) relative to the 2050 CLE case, contributing around one-thirds of the total peak season MDA8 reduction (13.7 µg m$^{-3}$, or 15.4 %). The other two-thirds are split almost equally between the impact of other precursor ($NO_x$, CO, NMVOC) emission reductions in the EMEP and ROW regions, respectively. As for $CH_4$, the impact of further abatement policies for the other precursor emissions is comparatively small in the LOW scenario. Focusing therefore on the comparison between the 2050 CLE and MFR scenarios, our results highlight that reducing $CH_4$ emissions has the potential to lead to substantial peak season MDA8 reductions, having a similarly strong effect as the reduction of other precursor emissions within the EMEP region. The $CH_4$ reductions are, however, almost entirely the result of, and can only be achieved by, $CH_4$ emission reductions outside of the EMEP region. Moreover, relative to the 2015 baseline, the increasing $CH_4$ concentrations in the 2050 CLE scenario partly offset (+3.1 µg m$^{-3}$) the peak season MDA8 reductions achieved by the CLE reductions of other precursor emissions in the EMEP region (-4.5 µg m$^{-3}$). This highlights that simultaneous reductions in $CH_4$ emissions helps to avoid offsetting the air pollution benefits already achieved by the (regional) CLE precursor emission reductions, while also playing an important role in bringing air pollution further down beyond the 2050 CLE scenario.

In terms of the total reductions, the 2050 MFR scenario brings the EMEP region average peak season MDA8 exposure down from 89.2 to 75.4 µg m$^{-3}$ relative to the CLE, against a 2015 baseline exposure of 92.0 µg m$^{-3}$. Nevertheless, in the MFR scenario the majority of countries in the EMEP region (38 out of 49) are projected to stay above the interim WHO exposure target of 70 µg m$^{-3}$. While the more stringent emission policies of the LOW scenario reduces the number of countries to 30, it still highlights the difficulties in reaching WHO guideline values, given also that even in the LOW scenario none of the countries fall below the 60 µg m$^{-3}$ WHO limit. However, our results may be regarded as somewhat of an upper estimate, as the comparison against observations across Europe found the model to overestimate peak season MDA8 by 3.8 % (3.2 µg m$^{-3}$) on average in the 2015 baseline emission scenario.

While the current work focuses on the peak season MDA8 indicator, the scenario results are also discussed for a range of other health and vegetation $O_3$ indicators. These results find that the relative importance of $CH_4$ and other precursor emission reductions depends on the choice of indicator, and to some extent on the spatial averaging approach (area or population weighted). Nevertheless, $O_3$ indicators emphasizing peak $O_3$ concentrations (e.g., SOMO35, JJA $O_3$ max, 4th MDA8) yield results largely consistent with those for peak season MDA8 in terms of the relative importance of the different emission changes. The scenario percentage change impacts can vary considerably between the different indicators, however, being mostly dependent on the extent to which a threshold value applies. For example, the total reduction between the CLE and MFR scenarios

520   for the SOMO35 health indicator and the $POD_3IAM_{WH}$ vegetation indicator amounts to 53.3 % and 26.2 %, respectively, compared to a 15.4 % total reduction for peak season MDA8.

     The current work also highlights that reducing $CH_4$ emissions achieves considerable global warming reductions, with solely reducing $CH_4$ emissions achieving roughly two-thirds of the possible temperature reduction between the full 2050 CLE (SSP2-4.5 GHGs) and LOW (SSP1-2.6 GHGs) scenarios. However, as for the $CH_4$ air pollution benefits, the global warming reduc-

525   tions are almost entirely the result of $CH_4$ emission reductions outside of the EMEP region.

# References

Abernethy, S., O'Connor, F. M., Jones, C. D., and Jackson, R. B.: Methane removal and the proportional reductions in surface temperature and ozone, Philosophical Transactions of the Royal Society A: Mathematical, Physical and Engineering Sciences, 379, 20210 104, https://doi.org/10.1098/rsta.2021.0104, 2021.

555 Alexandratos, N. and Bruinsma, J.: World agriculture towards 2030/2050: the 2012 revision, ESA Working paper No. 12-03. Rome, FAO., https://www.fao.org/3/ap106e/ap106e.pdf, [Last access: April 2024], 2012.

Amann, M., Bertok, I., Borken-Kleefeld, J., Cofala, J., Heyes, C., Hoeglund-Isaksson, L., Klimont, Z., Nguyen, B., Posch, M., Rafaj, P., Sandler, R., Schoepp, W., Wagner, F., and Winiwarter, W.: Cost-effective control of air quality and greenhouse gases in Europe: Modeling and policy applications, Environmental Modelling & Software, 26, 1489–1501, https://doi.org/10.1016/j.envsoft.2011.07.012, 2011.

560 Amann, M., Klimont, Z., and Wagner, F.: Regional and Global Emissions of Air Pollutants: Recent Trends and Future Scenarios, Annual Review of Environment and Resources, 38, 31–55, https://doi.org/10.1146/annurev-environ-052912-173303, 2013.

Amann, M., Kiesewetter, G., Schöpp, W., Klimont, Z., Winiwarter, W., Cofala, J., Rafaj, P., Höglund-Isaksson, L., Gomez-Sabriana, A., Heyes, C., Purohit, P., Borken-Kleefeld, J., Wagner, F., Sander, R., Fagerli, H., Nyiri, A., Cozzi, L., and Pavarini, C.: Reducing global air pollution: the scope for further policy interventions, Philosophical transactions. Series A, Mathematical, physical, and engineering
565 sciences, 378, 20190 331, https://doi.org/10.1098/rsta.2019.0331, 2020.

Belis, C. A. and Van Dingenen, R.: Air quality and related health impact in the UNECE region: source attribution and scenario analysis, Atmospheric Chemistry and Physics, 23, 8225–8240, https://doi.org/10.5194/acp-23-8225-2023, 2023.

Bergström, R., Hayman, G. D., Jenkin, M. E., and Simpson, D.: Update and comparison of atmospheric chemistry mechanisms for the EMEP MSC-W model system, Tech. rep., https://emep.int/publ/reports/2022/MSCW_technical_1_2022.pdf, 2022.

570 Colette, A., Andersson, C., Baklanov, A., Bessagnet, B., Brandt, J., Christensen, J. H., Doherty, R., Engardt, M., Geels, C., Giannakopoulos, C., Hedegaard, G. B., Katragkou, E., Langner, J., Lei, H., Manders, A., Melas, D., Meleux, F., Rouïl, L., Sofiev, M., Soares, J., Stevenson, D. S., Tombrou-Tzella, M., Varotsos, K. V., and Young, P.: Is the ozone climate penalty robust in Europe?, Environmental Research Letters, 10, 084 015, https://doi.org/10.1088/1748-9326/10/8/084015, 2015.

Crutzen, P. J., Lawrence, M. G., and Pöschl, U.: On the background photochemistry of tropospheric ozone, Tellus B: Chemical and Physical
575 Meteorology, 51, 123–146, https://doi.org/10.3402/tellusb.v51i1.16264, 1999.

de Meij, A., Cuvelier, C., Thunis, P., Pisoni, E., and Bessagnet, B.: Sensitivity of air quality model responses to emission changes: comparison of results based on four EU inventories through FAIRMODE benchmarking methodology, Geoscientific Model Development, 17, 587–606, https://doi.org/10.5194/gmd-17-587-2024, 2024.

Dentener, F., Stevenson, D., Cofala, J., Mechler, R., Amann, M., Bergamaschi, P., Raes, F., and Derwent, R.: The impact of air pollutant
580 and methane emission controls on tropospheric ozone and radiative forcing: CTM calculations for the period 1990-2030, Atmospheric Chemistry and Physics, 5, 1731–1755, https://doi.org/10.5194/acp-5-1731-2005, 2005.

ECMWF: IFS Documentation CY40R1 - Part IV: Physical Processes, Tech. Rep. 4, ECMWF, https://doi.org/10.21957/f56vvey1x, 2014.

Emberson, L.: Effects of ozone on agriculture, forests and grasslands, Philosophical Transactions of the Royal Society A, 378, 20190 327, https://doi.org/10.1098/rsta.2019.0327, 2020.

585 EMEP MSC-W: OpenSource v5.0 (202310), https://doi.org/10.5281/zenodo.8431553, 2023.

EMEP/CEIP: Present state of emission data, https://www.ceip.at/webdab-emission-database/reported-emissiondata, [last access February 2024], 2023.

EU: Consolidated text: Directive 2008/50/EC of the European Parliament and of the Council of 21 May 2008 on ambient air quality and cleaner air for Europe, Tech. rep., Publications Office, https://eur-lex.europa.eu/EN/legal-content/summary/cleaner-air-for-europe.html, [Last Access: February 2024], 2008.

Fagerli, H., Tsyro, S., Jonson, J. E., and al et: Transboundary particulate matter, photo-oxidants, acidifying and eutrophying components. EMEP Status Report 1/2023, Tech. rep., The Norwegian Meteorological Institute, Oslo, Norway, available from www.emep.int [last access: March 2024], 2023.

Fiore, A. M., West, J. J., Horowitz, L. W., Naik, V., and Schwarzkopf, M. D.: Characterizing the tropospheric ozone response to methane emission controls and the benefits to climate and air quality, Journal of Geophysical Research: Atmospheres, 113, 2008.

Fleming, Z. L., Doherty, R. M., von Schneidemesser, E., Malley, C. S., Cooper, O. R., Pinto, J. P., Colette, A., Xu, X., Simpson, D., Schultz, M. G., Lefohn, A. S., Hamad, S., Moolla, R., Solberg, S., and Feng, Z.: Tropospheric Ozone Assessment Report: Present-day ozone distribution and trends relevant to human health, Elementa: Science of the Anthropocene, 6, 12, https://doi.org/10.1525/elementa.273, 2018.

Forster, P., Storelvmo, T., Armour, K., Collins, W., Dufresne, J.-L., Frame, D., Lunt, D., Mauritsen, T., Palmer, M., Watanabe, M., Wild, M., and Zhang, H.: The Earth's Energy Budget, Climate Feedbacks, and Climate Sensitivity. Climate Change 2021: The Physical Science Basis. Contribution of Working Group I to the Sixth Assessment Report of the Intergovernmental Panel on Climate Change, p. 923–1054, Cambridge University Press, Cambridge, United Kingdom and New York, NY, USA, https://doi.org/10.1017/9781009157896.009, 2021.

Fu, T.-M. and Tian, H.: Climate change penalty to ozone air quality: review of current understandings and knowledge gaps, Current Pollution Reports, 5, 159–171, 2019.

Ge, Y., Solberg, S., Heal, M. R., Reimann, S., van Caspel, W., Hellack, B., Salameh, T., and Simpson, D.: Evaluation of modelled versus observed non-methane volatile organic compounds at European Monitoring and Evaluation Programme sites in Europe, Atmospheric Chemistry and Physics, 24, 7699–7729, https://doi.org/10.5194/acp-24-7699-2024, 2024.

Gliss, J., Griesfeller, J., and Svennevik, H.: metno/pyaerocom: Release version 0.8.0, https://doi.org/10.5281/zenodo.4159570, 2020.

Gomez Sanabria, A., Kiesewetter, G., Klimont, Z., Schoepp, W., and Haberl, H.: Potential for future reductions of global GHG and air pollutants from circular waste management systems, Nature Communication, 13, https://doi.org/10.1038/s41467-021-27624-7, 2022.

Guevara, M., Jorba, O., Tena, C., Denier van der Gon, H., Kuenen, J., Elguindi, N., Darras, S., Granier, C., and Pérez García-Pando, C.: Copernicus Atmosphere Monitoring Service TEMPOral profiles for the Global domain version 2.1 (CAMS-GLOB-TEMPOv2.1), Copernicus Atmosphere Monitoring Service, ECCAD, https://doi.org/10.24380/ks45-9147, 2020a.

Guevara, M., Jorba, O., Tena, C., Denier van der Gon, H., Kuenen, J., Elguindi, N., Darras, S., Granier, C., and Pérez García-Pando, C.: Copernicus Atmosphere Monitoring Service TEMPOral profiles for the regional European domain version 2.1 (CAMS-REG-TEMPOv2.1), Copernicus Atmosphere Monitoring Service, ECCAD, https://doi.org/10.24380/1cx4-zy68, 2020b.

Guevara, M., Jorba, O., Tena, C., Denier van der Gon, H., Kuenen, J., Elguindi, N., Darras, S., Granier, C., and Pérez García-Pando, C.: Copernicus Atmosphere Monitoring Service TEMPOral profiles (CAMS-TEMPO): global and European emission temporal profile maps for atmospheric chemistry modelling, Earth System Science Data, 13, 367–404, https://doi.org/10.5194/essd-13-367-2021, 2021.

Guo, J., Feng, H., Peng, C., Chen, H., Xu, X., Ma, X., Li, L., Kneeshaw, D., Ruan, H., Yang, H., and Wang, W.: Global Climate Change Increases Terrestrial Soil CH4 Emissions, Global Biogeochemical Cycles, 37, e2021GB007 255, https://doi.org/10.1029/2021GB007255, 2023.

He, X., Shen, W., Wallington, T. J., Zhang, S., Wu, X., Bao, Z., and Wu, Y.: Asia Pacific road transportation emissions, 1900–2050, Faraday Discuss., 226, 53–73, https://doi.org/10.1039/D0FD00096E, 2021.

Holmes, C. D., Prather, M. J., Søvde, O. A., and Myhre, G.: Future methane, hydroxyl, and their uncertainties: key climate and emission parameters for future predictions, Atmospheric Chemistry and Physics, 13, 285–302, https://doi.org/10.5194/acp-13-285-2013, 2013.

Huangfu, P. and Atkinson, R.: Long-term exposure to NO2 and O3 and all-cause and respiratory mortality: A systematic review and meta-analysis, Environment international, 144, 105 998, 2020.

630 Höglund-Isaksson, L.: Global anthropogenic methane emissions 2005-2030: technical mitigation potentials and costs, acpd, p. 11275–11315, 2012.

Höglund-Isaksson, L., Gómez-Sanabria, A., Klimont, Z., Rafaj, P., and Schöpp, W.: Technical potentials and costs for reducing global anthropogenic methane emissions in the 2050 timeframe –results from the GAINS model, Environmental Research Communications, 2, 025 004, https://doi.org/10.1088/2515-7620/ab7457, 2020.

635 IEA: World Energy Outlook 2018, https://www.iea.org/reports/world-energy-outlook-2018, [Last access: April 2024], 2018.

Isaksen, I. S. A., Berntsen, T. K., Dalsøren, S. B., Eleftheratos, K., Orsolini, Y., Rognerud, B., Stordal, F., Søvde, O. A., Zerefos, C., and Holmes, C. D.: Atmospheric Ozone and Methane in a Changing Climate, Atmosphere, 5, 518–535, https://doi.org/10.3390/atmos5030518, 2014.

Jonson, J. E., Schulz, M., Emmons, L., Flemming, J., Henze, D., Sudo, K., Lund, M. T., Lin, M., Benedictow, A., Koffi, B., Dentener, F.,
640 Keating, T., Kivi, R., and Davila, Y.: The effects of intercontinental emission sources on European air pollution levels, acp, 18, 13 655–13 672, https://doi.org/10.5194/acp-18-13655-2018, 2018.

Kanter, D. R., Winiwarter, W., Bodirsky, B. L., Bouwman, L., Boyer, E., Buckle, S., Compton, J. E., Dalgaard, T., de Vries, W., Leclère, D., Leip, A., Müller, C., Popp, A., Raghuram, N., Rao, S., Sutton, M. A., Tian, H., Westhoek, H., Zhang, X., and Zurek, M.: A framework for nitrogen futures in the shared socioeconomic pathways, Global Environmental Change, 61, 102 029,
645 https://doi.org/10.1016/j.gloenvcha.2019.102029, 2020.

Klimont, Z., Kupiainen, K., Heyes, C., Purohit, P., Cofala, J., Rafaj, P., Borken-Kleefeld, J., and Schöpp, W.: Global anthropogenic emissions of particulate matter including black carbon, Atmospheric Chemistry and Physics, 17, 8681–8723, https://doi.org/10.5194/acp-17-8681-2017, 2017.

Laj, P., Myhre, C. L., Riffault, V., Amiridis, V., Fuchs, H., Eleftheriadis, K., Petäjä, T., Salameh, T., Kivekäs, N., Juurola, E., Saponaro, G.,
650 Philippin, S., Cornacchia, C., Arboledas, L. A., Baars, H., Claude, A., Mazière, M. D., Dils, B., Dufresne, M., Evangeliou, N., Favez, O., Fiebig, M., Haeffelin, M., Herrmann, H., Höhler, K., Illmann, N., Kreuter, A., Ludewig, E., Marinou, E., Möhler, O., Mona, L., Murberg, L. E., Nicolae, D., Novelli, A., O'Connor, E., Ohneiser, K., Altieri, R. M. P., Picquet-Varrault, B., van Pinxteren, D., Pospichal, B., Putaud, J.-P., Reimann, S., Siomos, N., Stachlewska, I., Tillmann, R., Voudouri, K. A., Wandinger, U., Wiedensohler, A., Apituley, A., Comerón, A., Gysel-Beer, M., Mihalopoulos, N., Nikolova, N., Pietruczuk, A., Sauvage, S., Sciare, J., Skov, H., Svendby, T., Swietlicki, E., Tonev,
655 D., Vaughan, G., Zdimal, V., Baltensperger, U., Doussin, J.-F., Kulmala, M., Pappalardo, G., Sundet, S. S., and Vana, M.: Aerosol, Clouds and Trace Gases Research Infrastructure (ACTRIS): The European Research Infrastructure Supporting Atmospheric Science, Bulletin of the American Meteorological Society, 105, E1098 – E1136, https://doi.org/10.1175/BAMS-D-23-0064.1, 2024.

Lan, X., Thoning, K., and Dlugokencky, E.: Trends in globally-averaged CH4, N2O, and SF6 determined from NOAA Global Monitoring Laboratory measurements. Version 2024-07, https://doi.org/10.15138/P8XG-AA10, 2024.

660 Lefohn, A. S., Malley, C. S., Smith, L., Wells, B., Hazucha, M., Simon, H., Naik, V., Mills, G., Schultz, M. G., Paoletti, E., De Marco, A., Xu, X., Zhang, L., Wang, T., Neufeld, H. S., Musselman, R. C., Tarasick, D., Brauer, M., Feng, Z., Tang, H., Kobayashi, K., Sicard, P., Solberg, S., and Gerosa, G.: Tropospheric ozone assessment report: Global ozone metrics for climate change, human health, and crop/ecosystem research, Elementa: Science of the Anthropocene, 6, 27, https://doi.org/10.1525/elementa.279, 2018.

Malley, C. S., Borgford-Parnell, N., Haeussling, S., Howard, I. C., Lefèvre, E. N., and Kuylenstierna, J. C. I.: A roadmap to achieve the global methane pledge, Environmental Research: Climate, 2, 011 003, https://doi.org/10.1088/2752-5295/acb4b4, 2023.

Mar, K. A., Unger, C., Walderdorff, L., and Butler, T.: Beyond CO2 equivalence: The impacts of methane on climate, ecosystems, and health, Environmental Science & Policy, 134, 127–136, https://doi.org/10.1016/j.envsci.2022.03.027, 2022.

Meinshausen, M., Meinshausen, N., Hare, W., Raper, S. C., Frieler, K., Knutti, R., Frame, D. J., and Allen, M. R.: Greenhouse-gas emission targets for limiting global warming to 2 C, Nature, 458, 1158–1162, https://doi.org/10.1038/nature08017, 2009.

Meinshausen, M., Raper, S. C. B., and Wigley, T. M. L.: Emulating coupled atmosphere-ocean and carbon cycle models with a simpler model, MAGICC6 – Part 1: Model description and calibration, Atmospheric Chemistry and Physics, 11, 1417–1456, https://doi.org/10.5194/acp-11-1417-2011, 2011.

Meinshausen, M., Vogel, E., Nauels, A., Lorbacher, K., Meinshausen, N., Etheridge, D. M., Fraser, P. J., Montzka, S. A., Rayner, P. J., Trudinger, C. M., Krummel, P. B., Beyerle, U., Canadell, J. G., Daniel, J. S., Enting, I. G., Law, R. M., Lunder, C. R., O'Doherty, S., Prinn, R. G., Reimann, S., Rubino, M., Velders, G. J. M., Vollmer, M. K., Wang, R. H. J., and Weiss, R.: Historical greenhouse gas concentrations for climate modelling (CMIP6), Geoscientific Model Development, 10, 2057–2116, https://doi.org/10.5194/gmd-10-2057-2017, 2017.

Meinshausen, M., Nicholls, Z. R. J., Lewis, J., Gidden, M. J., Vogel, E., Freund, M., Beyerle, U., Gessner, C., Nauels, A., Bauer, N., Canadell, J. G., Daniel, J. S., John, A., Krummel, P. B., Luderer, G., Meinshausen, N., Montzka, S. A., Rayner, P. J., Reimann, S., Smith, S. J., van den Berg, M., Velders, G. J. M., Vollmer, M. K., and Wang, R. H. J.: The shared socio-economic pathway (SSP) greenhouse gas concentrations and their extensions to 2500, Geoscientific Model Development, 13, 3571–3605, https://doi.org/10.5194/gmd-13-3571-2020, 2020.

Mills, G., Sharps, K., Simpson, D., Pleijel, H., Broberg, M., Uddling, J., Jaramillo, F., Davies, W. J., Dentener, F., Van den Berg, M., et al.: Ozone pollution will compromise efforts to increase global wheat production, Global change biology, 24, 3560–3574, https://doi.org/10.1111/gcb.14157, 2018.

Monks, P. S., Archibald, A., Colette, A., Cooper, O., Coyle, M., Derwent, R., Fowler, D., Granier, C., Law, K. S., Mills, G., et al.: Tropospheric ozone and its precursors from the urban to the global scale from air quality to short-lived climate forcer, Atmospheric Chemistry and Physics, 15, 8889–8973, https://doi.org/10.5194/acp-15-8889-2015, 2015.

Nicholls, Z., Meinshausen, M., Lewis, J., Corradi, M. R., Dorheim, K., Gasser, T., Gieseke, R., Hope, A. P., Leach, N. J., McBride, L. A., Quilcaille, Y., Rogelj, J., Salawitch, R. J., Samset, B. H., Sandstad, M., Shiklomanov, A., Skeie, R. B., Smith, C. J., Smith, S. J., Su, X., Tsutsui, J., Vega-Westhoff, B., and Woodard, D. L.: Reduced Complexity Model Intercomparison Project Phase 2: Synthesizing Earth System Knowledge for Probabilistic Climate Projections, Earth's Future, 9, e2020EF001 900, https://doi.org/10.1029/2020EF001900, 2021.

Nicholls, Z., Meinshausen, M., Lewis, J., Smith, C. J., Forster, P. M., Fuglestvedt, J. S., Rogelj, J., Kikstra, J. S., Riahi, K., and Byers, E.: Changes in IPCC Scenario Assessment Emulators Between SR1.5 and AR6 Unraveled, Geophysical Research Letters, 49, e2022GL099 788, https://doi.org/10.1029/2022GL099788, e2022GL099788 2022GL099788, 2022.

Nicholls, Z. R. J., Meinshausen, M., Lewis, J., Gieseke, R., Dommenget, D., Dorheim, K., Fan, C.-S., Fuglestvedt, J. S., Gasser, T., Golüke, U., Goodwin, P., Hartin, C., Hope, A. P., Kriegler, E., Leach, N. J., Marchegiani, D., McBride, L. A., Quilcaille, Y., Rogelj, J., Salawitch, R. J., Samset, B. H., Sandstad, M., Shiklomanov, A. N., Skeie, R. B., Smith, C. J., Smith, S., Tanaka, K., Tsutsui, J., and Xie, Z.: Reduced Complexity Model Intercomparison Project Phase 1: introduction and evaluation of global-mean temperature response, Geoscientific Model Development, 13, 5175–5190, https://doi.org/10.5194/gmd-13-5175-2020, 2020.

O'Neill, B. C., Kriegler, E., Ebi, K. L., Kemp-Benedict, E., Riahi, K., Rothman, D. S., van Ruijven, B. J., van Vuuren, D. P., Birkmann, J., Kok, K., Levy, M., and Solecki, W.: The roads ahead: Narratives for shared socioeconomic pathways describing world futures in the 21st century, Global Environmental Change, 42, 169–180, https://doi.org/10.1016/j.gloenvcha.2015.01.004, 2017.

Pandey, D., Sharps, K., Simpson, D., Ramaswami, B., Cremades, R., Booth, N., Jamir, C., Büker, P., Sinha, V., Sinha, B., et al.: Assessing the costs of ozone pollution in India for wheat producers, consumers, and government food welfare policies, Proceedings of the National Academy of Sciences, 120, e2207081 120, https://doi.org/10.1073/pnas.2207081120, 2023.

Rafaj, P., Kiesewetter, G., Gül, T., Schöpp, W., Cofala, J., Klimont, Z., Purohit, P., Heyes, C., Amann, M., B.-K., and J., Cozzi, L.: Outlook for clean air in the context of sustainable development goals, Glob. Environ. Change, 53, 1–11, https://doi.org/10.1016/j.gloenvcha.2018.08.008, 2018.

Rasmussen, D., Hu, J., Mahmud, A., and Kleeman, M. J.: The ozone–climate penalty: past, present, and future, Environmental science & technology, 47, 14 258–14 266, 2013.

Riahi, K., van Vuuren, D. P., Kriegler, E., Edmonds, J., O'Neill, B. C., Fujimori, S., Bauer, N., Calvin, K., Dellink, R., Fricko, O., Lutz, W., Popp, A., Cuaresma, J. C., KC, S., Leimbach, M., Jiang, L., Kram, T., Rao, S., Emmerling, J., Ebi, K., Hasegawa, T., Havlik, P., Humpenöder, F., Da Silva, L. A., Smith, S., Stehfest, E., Bosetti, V., Eom, J., Gernaat, D., Masui, T., Rogelj, J., Strefler, J., Drouet, L., Krey, V., Luderer, G., Harmsen, M., Takahashi, K., Baumstark, L., Doelman, J. C., Kainuma, M., Klimont, Z., Marangoni, G., Lotze-Campen, H., Obersteiner, M., Tabeau, A., and Tavoni, M.: The Shared Socioeconomic Pathways and their energy, land use, and greenhouse gas emissions implications: An overview, Global Environmental Change, 42, 153–168, https://doi.org/10.1016/j.gloenvcha.2016.05.009, 2017.

Saunois, M., Stavert, A. R., Poulter, B., Bousquet, P., Canadell, J. G., Jackson, R. B., Raymond, P. A., Dlugokencky, E. J., Houweling, S., Patra, P. K., Ciais, P., Arora, V. K., Bastviken, D., Bergamaschi, P., Blake, D. R., Brailsford, G., Bruhwiler, L., Carlson, K. M., Carrol, M., Castaldi, S., Chandra, N., Crevoisier, C., Crill, P. M., Covey, K., Curry, C. L., Etiope, G., Frankenberg, C., Gedney, N., Hegglin, M. I., Höglund-Isaksson, L., Hugelius, G., Ishizawa, M., Ito, A., Janssens-Maenhout, G., Jensen, K. M., Joos, F., Kleinen, T., Krummel, P. B., Langenfelds, R. L., Laruelle, G. G., Liu, L., Machida, T., Maksyutov, S., McDonald, K. C., McNorton, J., Miller, P. A., Melton, J. R., Morino, I., Müller, J., Murguia-Flores, F., Naik, V., Niwa, Y., Noce, S., O'Doherty, S., Parker, R. J., Peng, C., Peng, S., Peters, G. P., Prigent, C., Prinn, R., Ramonet, M., Regnier, P., Riley, W. J., Rosentreter, J. A., Segers, A., Simpson, I. J., Shi, H., Smith, S. J., Steele, L. P., Thornton, B. F., Tian, H., Tohjima, Y., Tubiello, F. N., Tsuruta, A., Viovy, N., Voulgarakis, A., Weber, T. S., van Weele, M., van der Werf, G. R., Weiss, R. F., Worthy, D., Wunch, D., Yin, Y., Yoshida, Y., Zhang, W., Zhang, Z., Zhao, Y., Zheng, B., Zhu, Q., Zhu, Q., and Zhuang, Q.: The Global Methane Budget 2000–2017, Earth System Science Data, 12, 1561–1623, https://doi.org/10.5194/essd-12-1561-2020, 2020.

Schiavina, M., Melchiorri, M., Pesaresi, M., Politis, P., Carneiro Freire, S., Maffenini, L., Florio, P., Ehrlich, D., Goch, K., Carioli, A., Uhl, J., Tommasi, P., and Kemper, T.: GHSL Data Package 2023, Publications Office of the European Union, https://doi.org/10.2760/098587, 2023.

Schneider von Deimling, T., Meinshausen, M., Levermann, A., Huber, V., Frieler, K., Lawrence, D. M., and Brovkin, V.: Estimating the near-surface permafrost-carbon feedback on global warming, Biogeosciences, 9, 649–665, https://doi.org/10.5194/bg-9-649-2012, 2012.

Simpson, D.: The EMEP MSC-W modelling programme: Its relationship to policy support, current challenges and future perspectives, in: Air Pollution Modelling and its Application XXII, edited by Steyn, D., Builtjes, P., and Timmermans, R., NATO Science for Peace and Security Series C. Environmental Security, pp. 265–268, Springer, Dordrecht, 32nd NATO/SPS International Technical Meeting, 2013.

Simpson, D. and Darras, S.: Global soil NO emissions for Atmospheric Chemical Transport Modelling: CAMS-GLOB-SOIL v2.2, Earth System Science Data Discussions, 2021, 1–35, https://doi.org/10.5194/essd-2021-221, 2021.

740  Simpson, D., Ashmore, M., Emberson, L., and Tuovinen, J.-P.: A comparison of two different approaches for mapping potential ozone damage to vegetation. A model study, Environmental Pollution, 146, 715–725, https://doi.org/10.1016/j.envpol.2006.04.013, critcial Levels for Ozone Effects on Vegetation: Further Applying and Developing the Flux Concept, 2007.

Simpson, D., Benedictow, A., Berge, H., Bergström, R., Emberson, L. D., Fagerli, H., Flechard, C. R., Hayman, G. D., Gauss, M., Jonson, J. E., Jenkin, M. E., Nyíri, A., Richter, C., Semeena, V. S., Tsyro, S., Tuovinen, J.-P., Valdebenito, A., and Wind, P.: The EMEP MSC-W

745  chemical transport model — technical description, Atmospheric Chemistry and Physics, 12, 7825–7865, https://doi.org/10.5194/acp-12-7825-2012, 2012.

Simpson, D., Tsyro, S., and Wind, P.: Updates to the EMEP/MSC-W model, in: Transboundary particulate matter, photo-oxidants, acidifying and eutrophying components. EMEP Status Report 1/2015, pp. 129–138, The Norwegian Meteorological Institute, Oslo, Norway, https://emep.int/publ/reports/2015/EMEP_Status_Report_1_2015.pdf, [last access: July 2024], 2015.

750  Stadtler, S., Simpson, D., Schröder, S., Taraborrelli, D., Bott, A., and Schultz, M.: Ozone impacts of gas–aerosol uptake in global chemistry-transport models, acp, 18, 3147–3171, https://doi.org/10.5194/acp-18-3147-2018, 2018.

The Food and Land Use Coalition: Growing Better: Ten Critical Transitions to Transform Food and Land Use, https://www.foodandlandusecoalition.org/, 2019.

Thunis, P., Clappier, A., Pisoni, E., Bessagnet, B., Kuenen, J., Guevara, M., and Lopez-Aparicio, S.: A multi-pollutant and

755  multi-sectorial approach to screening the consistency of emission inventories, Geoscientific Model Development, 15, 5271–5286, https://doi.org/10.5194/gmd-15-5271-2022, 2022.

Tørseth, K., Aas, W., Breivik, K., Fjæraa, A. M., Fiebig, M., Hjellbrekke, A. G., Lund Myhre, C., Solberg, S., and Yttri, K. E.: Introduction to the European Monitoring and Evaluation Programme (EMEP) and observed atmospheric composition change during 1972&ndash;2009, Atmospheric Chemistry and Physics, 12, 5447–5481, https://doi.org/10.5194/acp-12-5447-2012, 2012.

760  Turnock, S. T., Wild, O., Dentener, F. J., Davila, Y., Emmons, L. K., Flemming, J., Folberth, G. A., Henze, D. K., Jonson, J. E., Keating, T. J., Kengo, S., Lin, M., Lund, M., Tilmes, S., and O'Connor, F. M.: The impact of future emission policies on tropospheric ozone using a parameterised approach, Atmospheric Chemistry and Physics, 18, 8953–8978, https://doi.org/10.5194/acp-18-8953-2018, 2018.

UNECE: Mapping critical levels for vegetations. Revised Chapter 3 of the Manual on Methodologies and Criteria for Modelling and Mapping Critical Loads and Levels and Air Pollution Effects, Risks and Trends., ICP vegetation, CEH, UK, https://unece.org/fileadmin/DAM/env/

765  documents/2017/AIR/EMEP/Final__new_Chapter_3_v2__August_2017_.pdf, [last access: March 2024], 2017.

UNEP: United Nations Environment Programme and Climate and Clean Air Coalition. Global Methane Assessment: Benefits and Costs of Mitigating Methane Emissions., Nairobi: United Nations Environment Programme, ISBN: 978-92-807-3854-4, Job No: DTI/2352/PA, 2021.

van Caspel, W. E., Simpson, D., Jonson, J. E., Benedictow, A. M. K., Ge, Y., di Sarra, A., Pace, G., Vieno, M., Walker, H. L., and Heal,

770  M. R.: Implementation and evaluation of updated photolysis rates in the EMEP MSC-W chemistry-transport model using Cloud-$J$ v7.3e, Geoscientific Model Development, 16, 7433–7459, https://doi.org/10.5194/gmd-16-7433-2023, 2023.

van Caspel, W. E., Klimont, Z., Heyes, C., and Fagerli, H.: Dataset supporting the article: Impact of methane and other precursor emission reductions on surface ozone in Europe: Scenario analysis using the EMEP MSC-W model, https://doi.org/10.5281/zenodo.13287103, 2024.

775   WHO: WHO global air quality guidelines. Particulate Matter (PM2. 5 and PM10), Ozone, Nitrogen Dioxide, Sulfur Dioxide and Carbon Monoxide, World Health Organization Geneva, Switzerland, Licence: CC BY-NC-SA 3.0 IGO., 2021.

Wiedinmyer, C., Kimura, Y., McDonald-Buller, E. C., Emmons, L. K., Buchholz, R. R., Tang, W., Seto, K., Joseph, M. B., Barsanti, K. C., Carlton, A. G., and Yokelson, R.: The Fire Inventory from NCAR version 2.5: an updated global fire emissions model for climate and chemistry applications, EGUsphere, 2023, 1–45, https://doi.org/10.5194/egusphere-2023-124, 2023.

780   Willett, W., Rockström, J., Loken, B., Springmann, M., Lang, T., Vermeulen, S., Garnett, T., Tilman, D., DeClerck, F., Wood, A., et al.: Food in the Anthropocene: the EAT–Lancet Commission on healthy diets from sustainable food systems, The lancet, 393, 447–492, https://doi.org/10.1016/S0140-6736(18)31788-4, 2019.

Winiwarter, W., Höglund-Isaksson, L., Klimont, Z., Schöpp, W., and Amann, M.: Technical opportunities to reduce global anthropogenic emissions of nitrous oxide, Environmental Research Letters, 13, 014 011, https://doi.org/10.1088/1748-9326/aa9ec9, 2018.

785   Zhang, X.: Emission standards and control of PM2.5 from coal power plants (ISBN: 978–92–9029–590-7), IEA Clean Coal Centre, London, 2018.